Supplemental Information for Chemical transport models often underestimate inorganic aerosol acidity in remote regions of the atmosphere

Benjamin A. Nault, Pedro Campuzano-Jost, Douglas A. Day, Duseong S. Jo, Jason C. Schroder, Hannah M. Allen, Roya Bahreini, Huisheng Bian, Donald R. Blake, Mian Chin, Simon L. Clegg, Peter R. Colarco, John D. Crounse, Michael J. Cubison, Peter F. DeCarlo, Jack E. Dibb, Glenn S. Diskin, Alma Hodzic, Weiwei Hu, Joseph M. Katich, Michelle J. Kim, John K. Kodros, Agnieszka Kupc, Felipe D. Lopez-Hilfiker, Eloise A. Marais, Ann M. Middlebrook, J. Andrew Neuman, John B. Nowak, Brett B. Palm, Fabien Paulot, Jeffrey R. Pierce, Gregory P. Schill, Eric Scheuer, Joel A. Thornton, Kostas Tsigaridis, Paul O. Wennberg, Christina J. Williamson, and Jose L. Jimenez

Supplemental Information Section 1 - 6

Supplemental Information Tables 1 - 8

Supplemental Information Figures 1 - 31

S1 Constraints on Ammonia Mixing Ratio

Ammonia is the most important atmospheric base, and plays a critical role in controlling aerosol pH and ammonium balance[1], as discussed above. It also impacts new particle formation[2,3]. As discussed in Methods Section, even for campaigns missing ammonia measurements, an important constraint can be placed from our thermodynamic analysis for the potential mixing ratio of ammonia in the troposphere. For example, the point-to-point comparison for the CalNex case study is noisy, but, on average, the modeled ammonia is within a factor of 2 of the observed ammonia (Supplemental Figure 22 and 23). We expect this relative uncertainty to potentially increase for regions of low ammonia concentrations (i.e., remote locations) as most of the ammonia will be in the particle phase (Fig. 1c).

Generally, the estimated ammonia is low (<10 pptv) outside continental and biomass burning-influenced air over the Pacific and Atlantic Ocean (Supplemental Figure 9). This is in agreement with remote ammonia observations from satellites; though, the satellite detection limits (3 - 5 pptv) are higher than the low mixing ratios reported in Supplemental Figure 9. These low mixing ratios have two important implications. First, they further support low NH_x emissions and mixing ratios over oceanic regions[4] and that the lifetime of ammonia is short, preventing high mixing ratios throughout the remote atmosphere. Second, the ternary nucleation rates by sulfuric acid vapor, water vapor, and ammonia would be low, limiting new particle formation from this pathway[2]. The air masses with higher ammonia mixing ratios would have limited new particle formation due to higher particle number concentration and condensational sink[5]. This is in agreement with ammonia being unlikely to explain the observed new particle formation observed over these oceanic basins during ATom-1 and -2[5].

Over the continents (Supplemental Figure 9), there is high ammonia for regions affected by agriculture and anthropogenic activities[1,6]. In the upper troposphere and boreal forest, though, in the absence of biomass burning plumes, there is minimal ammonia, further indicating (a) boreal forests are a small source of ammonia[6] and (b) although convection can transport ammonia[7], it is short-lived and the resulting mixing ratios are still low compared to the boundary layer and lower free troposphere. Similar to over the oceans, the regions with higher ammonia gas mixing ratios would have limited new particle formation due to the high aerosol mass concentrations observed (Fig. 4).

The CTMs that include ammonia show relatively high biases both over the ocean basins and over the continents (Supplemental Figure 9). Further, the models show orders of magnitude higher ammonia in the free troposphere than what has been observed by satellite[7,8] or other remote sensing instruments[9]. This points to two important uncertainties in the CTMs: (a) high biases in ammonia emissions from oceans[4], as the oceanic boundary layer has $1-2$ orders of magnitude higher ammonia than the observationally-constrained ammonia value; and, (b) too long of ammonia lifetime, as the concentrations remain high throughout the troposphere. Thus, these two uncertainties are potentially driving the high bias in ammonium balance between models and observations discussed throughout the manuscript and can impact the understanding of new particle formation in the remote regions around the world.

S2 Calculation of Hygroscopic Growth Factors

The hygroscopic growth factors (HGF) were calculated to investigate how the inorganic aerosol composition impacted water uptake and in turn diameter. This value has important

implications for direct radiative effect as ammonium-sulfate-like versus sulfuric-acid-like aerosols have different values[10]. We estimated the HGF for every minute of flights for all campaigns; then, we plotted and binned the calculated HGF data as a function of RH and NH_{4_Bal}. To calculate the HGF, the total inorganic volume, measured by AMS (sulfate, nitrate, and ammonium), was added to the volume from water, which was estimated by E-AIM:

$$HGF = \left(\frac{volume_{water} + volume_{dry,aerosol}}{volume_{dry,aerosol}}\right)^{1/3} \quad \text{Eq. S1}$$

The dry aerosol volume was calculated by assuming a density of 1.78 g cm^{-3} for ammonium, nitrate, and sulfate[11,12]. Only inorganics were considered in Eq. S1 for consistency with the GEOS-Chem DRE calculation, which assumes an external mixture of the aerosol components[13].

The HGF, calculated from all the campaigns (Supplemental Table 2), were binned against RH and NH_{4_Bal}. The dependence of HGF for T was smaller versus RH, as E-AIM operated with the metastable assumption, making the aerosol liquid water more dependent on RH than T (and thus not shown). The HGF shown in Supplemental Figure 6 for the CTMs was calculated by using the average RH and NH_{4_Bal} to estimate the HGF from the look up table (Supplemental Figure 5).

S3 Theoretical E-AIM Calculation to Investigate Impact of RH and Aerosol Composition on Ammonium Balance and pH

Here, we describe a simple sensitivity study in the role of RH and aerosol composition on aerosol pH. These sensitivity calculations were designed to study the large variation in relative responses between NH_{4_Bal} and pH shown in Fig. 3. We adapted the theoretical model described by Murphy et al.[14]. Similar to Murphy et al.[14], total ammonium ($NH_{3,g}$ + $NH_4^+{}_{,p}$) was kept

constant at 200 nmol m^{-3}, sulfate was varied between 5 to 1000 nmol m^{-3}, total nitrate ($HNO_{3,g}$ + $NO_3^-{}_{,p}$) was kept constant at 0.01 nmol m^{-3}, and RH varied between 30 to 95%. We performed the simulations for two temperatures, 298 and 243 K. The same E-AIM (Model IV) and definition of pH was used here as throughout the paper. This is a significant difference compared to Murphy et al.[14], in that they used the pH definition based on the mole fraction of H^+ instead of molality of H^+. The results of the model are described in the main text.

S4 Comparison of Volatile and Non-Volatile Volume Distribution, Description of Condensational Sink Calculation, Description of Estimated Sea-Salt/Sodium and of Other Cations, and Importance of Non-Volatile Cations

Here, we investigate the importance of non-volatile cations (NVCs) in fine mode aerosol and any potential impact NVCs may have on NH_{4_Bal} and pH. During ATom-1 and -2, the AMS measured sea-salt in the marine boundary layer[15], using the techniques described in Ovadnevaite et al.[16]. However, this measurement does not provide information on whether the sea-salt was internally or externally mixed with sulfate-organic dominated fine mode aerosol. The following section investigates whether the sea-salt is internally or externally mixed into the fine aerosol and any potential error in assuming sea-salt is externally mixed into the sulfate-organic dominated fine mode aerosol. The summary of this section is that there are two main modes: (1) fine mode, dominated by sulfate and organics, and minimal NVCs. Any NVCs are externally mixed, and even if they were internally mixed, they would have minimal impact on NH_{4_Bal} and pH. (2) The coarse mode, dominated by NVC, would subsequently have a different pH. The focus of the paper is the fine mode aerosol..

105

106 **S4.1 Comparison of Volume Distributions**

107 Here we discuss comparisons of volatile versus non-volatile (refractory) volume
108 distributions measured during ATom, to investigate the mixing state of NVCs as well as their
109 importance to AMS measurements and condensation of acidic gases (e.g., sulfuric acid) in the
110 MBL. Condensing onto aerosol containing the NVCs would lead to the formation of non-volatile
111 salts, such as sodium sulfate or calcium sulfate, while condensing onto other aerosol would lead
112 to formation of ammonium salts or acidic aerosol (the focus of this study). During ATom-2, a set
113 of instruments, ultra-high-sensitivity aerosol size spectrometers (UHSAS), were used to
114 measured the size distribution of particles from 63 to 1000 nm (> 90% counting efficiency) and
115 the remaining aerosol number concentrations (i.e., aerosol containing non-volatile cations) after
116 heating the aerosol with a 300°C thermodenuder installed upstream with a residence time of 1.59
117 to 3.7 s, for the same diameter range[17,18]. As shown in Supplemental Figure 13a and b, there are
118 two populations in the aerosol volume — between 100 to 400 nm diameter and > 600 nm
119 diameter. A much larger fraction of the non-volatile components are at larger sizes, suggesting a
120 high degree of external mixing of those components, similar to what Guo et al. suggested[19]. A
121 large fraction of the aerosol volume at > 600 nm is non-volatile, as it is measured by the denuded
122 instrument, which is outside the range of aerosol measured by the AMS[20]. On the other hand, the
123 majority of the aerosol between 200 to 400 nm, the size range measured by the AMS and used
124 for the acidity calculations, is volatile. This is similar to what was observed by Murphy et al.[21],
125 where they found most of the sea-salt volume occurs above 600 nm diameter. Finally, the volume
126 of refractory aerosol (e.g., sea-salt) in the size range of the AMS (Supplemental Figure 13) is

likely overestimated due to sea-salt being externally mixed[22,23] and some fraction of the sizes after denuding are smaller than in the atmosphere due to loss of some volatile material from primary emissions[24].

S4.2 Calculation of the Condensational Sink

The condensational sink provided by the ambient aerosol is used for calculating the condensational sink of sulfuric acid to determine whether it is internally or externally mixed with sea-salt. The instruments used for this analysis are described above. The thermodenuder channel measured non-volatile, refractory components of the aerosol, which includes sea-salt and black carbon. The particle number size distributions of both UHSASs were used to calculate the condensational sink for the total aerosol and the refractory aerosol. The calculations described in Palm et al.[25] were used to estimate the condensational sink. Briefly, the condensational sink was calculated with Eq. S2:

$$CS = \int_0^\infty r\beta(r)N(r)dr \qquad \text{Eq. S2}$$

where the integral is the first moment of the particle size distribution, r is the wet particle radius, $N(r)$ is the particle number size distribution measured by either UHSAS, and

$$\beta(r) = \frac{Kn + 1}{0.377Kn + 1 + \frac{4}{3}\alpha^{-1}Kn^2 + \frac{4}{3}\alpha^{-1}Kn} \qquad \text{Eq. S3}$$

is the Fuchs-Sutugin correction[26]. This corrects the mass transfer of the condensing gas (i.e., sulfuric acid) to the particle surface in the transition regime. α is the sticking coefficient of the condensing species to the aerosol, which is assumed to be 1[27]. β(r) (Eq. S3) is a function of the Knudsen number:

$$Kn = \frac{\lambda_g}{r} \quad \text{Eq. S4}$$

where λ_g is the mean free path of the condensing gas. Finally, a growth factor of 1 is assumed here (no aerosol liquid water), which will be an underestimation of the condensational sink as water will increase the radius of the aerosol. However, due to limited chemical information for the aerosol composition < 100 nm and uncertainty on the amount of internal versus external mixing for the particle size distribution measured in the refractory channel, the assumption of 1 provides the most robust comparison.

S4.3 Comparison of Condensational Sink Distribution

As the condensational sink is dependent on aerosol surface area and is also higher for smaller particles in the free-molecular regime, it is weighed towards smaller diameters. This means that the overall condensational sink is dominated by the volatile, non-denuded aerosol (Supplemental Figure 13c and d) for diameters less than 600 nm, which is in the range of the AMS detection. Thus, the condensation of sulfuric acid onto aerosol is expected to preferentially occur onto aerosol containing non-volatile (refractory) aerosol, i.e., that observed by AMS. Therefore, for models that calculate aerosol pH on-line with a thermodynamic model and input all inorganic aerosol (sulfate, nitrate, ammonium, and submicron or accumulation mode sea-salt) and assume the inorganic aerosol are all internally mixed appear to not reflect the real atmosphere and lead to the higher aerosol pH, which would affect the predicted chemistry in regions of high sea-salt (e.g., Fig. 1). Finally, similar to volume distribution, condensational sink contributions of refractory aerosol (e.g., sea-salt) in the size range of the AMS (Supplemental Figure 13) is likely overestimated due to sea-salt being externally mixed[22,23] and some fraction of

the sizes after denuding are smaller than in the atmosphere due to loss of some volatile material from primary emissions.

S4.4 Description of Estimated Sea-Salt Volume/Mass Concentration Contribution

The UHSAS with a thermal denuder inlet was used to measure refractory aerosol number concentration and size. These data were used to estimate the integrated volume distribution of refractory particles during ATom-2 (see above). Black carbon was measured during ATom-2 by a single-particle soot photometer (SP2)[28]. The measured mass concentration was converted to volume concentration, assuming a density of 1.77 g cm^{-3} [29]. To estimate the sea-salt volume concentration, it was assumed the refractory volume concentration was composed of black carbon and sea-salt; thus, the sea-salt volume concentration was determined by difference between the refractory and black carbon volume. Then, the sodium mass concentration (Supplemental Figure 14) was estimated by assuming a sea-salt density of 1.45 g cm^{-3} [30] and assuming the chemical composition of sea-salt was approximately sodium chloride (NaCl).

S4.5 Importance of Non-Volatile Cations for PM_1

An important question is whether NVCs, including sodium (Na^+) from sea-salt, are internally mixed and thus should be included in calculating both pH and NH_{4_Bal}. In past studies, the inclusion of these NVCs was shown to mainly be important for aerosols larger than the AMS size range[19,20]. In this study, we focus on the pH of non-sea-salt-sulfate (NSS); the pH of sea-salt aerosols will be higher and is not analyzed here. Multiple pieces of evidence support the exclusion of sea-salt from the pH calculations of NSS sulfate: 1) the fraction of submicron Na^+

and sea-salt in the AMS size range is small, and even if it all was internally mixed with NSS sulfate, it would not perturb NH_{4_Bal} or pH much (NH_{4_Bal} by <1% and pH by 0.1 units, at most) due to the low Na^+ mass concentration (mean = 0.01 μg sm^{-3}) (Supplemental Figure 13 and Supplemental Figure 14); 2) sea-salt and NSS sulfate are externally mixed, due to (a) separate emission pathways for NSS sulfate[31] and NH_x[4] versus sea-salt[32] and to (b) sulfuric acid formed in the MBL condensing on the dominant condensational sink of NSS sulfate, and not on the sea-salt particles. Thus, for NSS sulfate[20], sea-salt should not be included for pH estimations. This leads to lower pH than estimated by models that include accumulation-mode sea-salt in the pH calculations (GEOS-Chem v10 and v12). Finally, as discussed in SI Sect. 4.6 (Supplemental Figure 15), the influence of other NVCs (such as K^+ and Ca^{2+}) on NH_{4_Bal} and pH is minimal, like Na^+; thus, for aerosols in the AMS size range, NVCs in general do not impact the conclusions discussed here.

In order to explore the large differences between models and observations in the BL, we look specifically at two recent versions of the GEOS-Chem model (v10 and v12). Above the BL, these two models capture both the trend (Supplemental Table 6) and probability distribution function (Supplemental Figure 12) of pH. GEOS-Chem, by default, includes accumulation mode sea-salt in the calculation of aerosol pH[33]. The short lifetime of sea-salt in GEOS-Chem[34] minimizes the vertical mixing of sea-salt into the free and upper troposphere, in line with the observations from Murphy et al.[21]. Therefore, the lack of sea-salt leads to better agreement between observations and GEOS-Chem above the BL; whereas, in the BL, the inclusion of sea-salt leads to the positive bias in the submicron aerosol pH (Fig. 3 and Supplemental Figure 12).

S4.6 Minimal Influence from Other Non-Volatile Cations

Besides sea-salt, other sources of NVCs include dust[19] and biomass burning[35]. Dust was rarely observed for particles smaller than 1 μm[36], except on one flight during ATom-1, where Saharan dust outflow was directly sampled. As discussed in Guo et al.[20], dust accounted for ~1% of PM_1 volume during ATom, meaning NVCs from dust generally would not impact the overall NH_{4_Bal} and pH calculated from observations. Potassium accounts for the majority of the NVC mass concentration for PM_1 from biomass burning[35,37]; however, as shown in Supplemental Figure 15, the median potassium concentration observed during campaigns focused on biomass burning (ARCTAS-B and SEAC^{4}RS) was < 0.10 μg sm^{-3} and for the ATom campaigns, ~0 μg sm^{-3}. This represents < 5% difference in NH_{4_Bal} and < 0.02 pH unit difference. Thus, for this study and the size-range of aerosol observed by the AMS, NVCs generally do not affect the NH_{4_Bal} and pH reported here.

S4.7 Minimal Partitioning of Ammonia to Sea-Salt (and Other Less Acidic Aerosol)

Another important aspect of sea-salt and other aerosols impacted by NVCs is that the pH is increased, which leads to lower partitioning of ammonia to the particle-phase[38]. Prior studies have observed that the pH for aerosol strongly impacted by sea-salt is >2[39–42], which generally leads to >90% of total NH_x (gas + particle) partitioning to the gas-phase[38]. Note, this aerosol is also mainly coarse aerosol. This has been further verified in that the aerosol with high sea-salt and high pH has minimal ammonium content[40–42]. Thus, it is expected that neglecting ammonium uptake for sea-salt aerosols will not bias the results described here.

S5 Sensitivity to Organic Contribution to Inorganic Mass Concentration

As the nominally inorganic ions measured by the AMS can in principle be produced from both inorganic and organic compounds in aerosol[43–46], a sensitivity analysis for each aerosol species reported from the AMS was conducted for its impacts on aerosol pH and NH_{4_Bal}.

S5.1 Potential Interference of Organic Oxidized Nitrogen Compounds on Nitrate

Organic oxidized nitrogen in aerosol are thought to be mainly organic nitrates ($pRONO_2$) outside biomass burning plumes[44,47,48], but can also include nitroaromatics[49] in biomass burning[50]. These species thermally decompose and fragment mainly into NO^+ and NO_2^+ ions, leading to a characteristic NO_x^+ ratio that is different than inorganic nitrate[43,44]. However, some of the campaigns used here did not perform this analysis, and for consistency we use the total reported nitrate as inorganic nitrate. Thus, the potential influence of this interference on the total nitrate is investigated.

Aerosol pH was calculated with the aerosol nitrate corrected for $pRONO_2$ for the SEAC[4]RS campaign, as this had a mixture of inorganic nitrate from biomass burning[51,52] and $pRONO_2$ from biogenic gas-phase chemistry[53]. The change in pH by removing $pRONO_2$ from the nitrate mass concentration, in general, is minimal, with a few point-to-point changes (Supplemental Figure 29). This is in agreement with the comparison of aerosol pH shown in Supplemental Figure 21, where there is minimal impact on the predicted aerosol pH upon using either AMS + CIMS total nitrate (particle nitrate, which includes $pRONO_2$, and HNO_3) or MC/IC total nitrate (particle nitrate, which should include minimal $pRONO_2$, and HNO_3). Though

hydrolysis of $pRONO_2$ is a potentially important sink that forms an alcohol and HNO_3 and a potential interference for MC/IC, most hydrolysis rates should be rapid enough to occur in the aerosol phase prior to sampling with the MC/IC[54]. Thus, it is not expected that $pRONO_2$ will substantially affect the total nitrate observed by the MC/IC. Therefore, it is not expected that inclusion of $pRONO_2$ has a large impact on the predicted pH, as over continental, polluted regions, most of the total nitrate is inorganic[55]; whereas, over clean, remote regions (i.e., ATom), nitrate composes a small fraction of the total inorganic mass concentration[36] and thus plays a small role in the thermodynamic calculations of aerosol and aerosol pH.

S5.2 Potential Interference of Organic Reduced Nitrogen Compounds on Ammonium

Organic reduced nitrogen compounds in aerosol, such as amines and pyridine, have been shown to contribute to charge balancing of sulfuric acid, especially for new particle formation events[56]. Further, amines have been suggested to potentially appear as total ammonium in the AMS due to thermal decomposition and ionization[45]. The influence of the organic reduced nitrogen compounds to ammonium balance and aerosol pH are investigated here.

Various organic reduced nitrogen compounds have been investigated in the AMS and compared against the NIST reference spectra[57]. It was found that the AMS spectra generally agreed with the NIST spectra. That means for cyclic organic reduced nitrogen compounds, such as pyridine, there is no contribution to the ammonium signal (NH^+, NH_2^+, NH_3^+)[58]. For amines, it is expected <2% of the total signal will be observed as ammonium signal[59]. Further, Ge et al.[57] observed that the majority of the amine signal between *m/z* 14 and 18 was due to $H_xO_y^+$ ions and not NH_x^+ ions. Thus, at the typical mass concentrations observed at the marine surface and

marine boundary layer (Supplemental Table 8), it is expected that, at most, 0.6 ng sm^{-3} ammonium would be observed due to oceanic amines. This is less than 2% of the observed average ammonium in the marine boundary layer during ATom-1 and -2 (42 and 49 ng sm^{-3}, respectively[36]). Thus, the amines have minimal impact on the measurement of ammonium balance in the marine boundary layer. It has been observed that the amines rapidly decrease with altitude[60], similar to methane sulfonic acid[61], with which amines are correlated[60]. Therefore, amines are expected to have an even smaller effect on ammonium balance outside the marine boundary layer (where ammonium concentrations were similar).

A more important way that the organic reduced nitrogen compounds could affect the results reported here is by acting as a base for the sulfuric acid. As shown in Supplemental Table 8 and Supplemental Figure 31, the estimated organic reduced nitrogen compounds account for a small fraction of the ammonium mass concentration (≤10% for amines and on average, <0.1% for pyridine). A sensitivity analysis was conducted, where it was assumed that the organic reduced nitrogen compounds behaved like ammonium, and the ammonium mass concentration was increased by 10% throughout ATom-2 (Supplemental Figure 30). Similar to the sensitivity analysis for $pRONO_2$, there is point-to-point variability in the predicted pH by increasing ammonium for potential organic reduced nitrogen compounds; however, the slope and average pH increase by a small amount (15% for slope and ~0.06 pH units for the average). Considering the best estimated uncertainty in pH is ~0.5 pH units[62,63], the majority of the data falls within this uncertainty (Supplemental Figure 30). Further, an upper estimate for organic reduced nitrogen compounds for all ammonium was considered, which should not be the case above the boundary layer[60], leading to an upper limit change in the predicted changes in aerosol pH. Thus, is it

expected that neglecting reduced nitrogen organic compounds will significantly impact the predicted pH reported here.

S5.3 Potential Interference of Organosulfates on Sulfate

Organosulfates have been shown to thermally decompose and ionize into various SO_x ions (i.e., SO^+, SO_2^+, SO_3^+, HSO_3^+, and $H_2SO_4^+$), impacting the total sulfate mass concentration[46]. In biogenic regions, the organosulfates may contribute a substantial fraction of the total sulfate mass concentration[64]. However, deconvolving the total sulfate signal into organic versus inorganic sulfate is difficult due to various matrix effects[46,65], making correction for this signal challenging. Though the fractional contribution of organosulfates to ground level total sulfate can be high occasionally at ground sites (>10%)[64], it has generally been found to be much lower for airborne observations (<7%)[66]. For example, during ATom, 1% or less of the sulfate was organosulfate, calculated from PALMS organosulfate and AMS sulfate mass concentrations, which would lead to a small change in the average sulfate mass concentration and thus to ammonium balance. Further, as described in Riva et al.[64], the majority of the campaigns used in this study are in locations with low epoxide to inorganic sulfate ratios, leading to minimal conversion of inorganic sulfate to organosulfate. Therefore, organosulfates are not expected to affect the reported ammonium balance and aerosol pH reported here.

S6 Comparison of Measured and E-AIM Modeled Volatile Species

Since accurate partitioning between gas-phase nitric acid and particle-phase nitrate indicates that the model predictions are reasonably accurate and hence the calculated aerosol pH is accurate to within ±0.5 pH[62,67] units (Fig. 1c), the model output was compared against

observations for all campaigns (Supplemental Figure 18 and 19). We found that for all but two campaigns (INTEX-B and ATom-2), the predicted versus observed gas-phase nitric acid and aerosol-phase nitrate were typically within the instrumental uncertainty of the observations (Supplemental Figure 20). For ATom-2, the total nitrate was low and near the AMS limit-of-detection[36]. From Fig. 1c, this would suggest extremely acidic aerosol, which is what is calculated by the model (Fig. 3 and Fig. 4). Thus, the low nitrate mass concentration is difficult to compare against the E-AIM model predictions, as this is near the noise of the measurement. The results presented are statistically similar (t-test) with and without INTEX-B and ATom-2.

As mentioned above, some campaigns had two measurements of total nitrate through CF_3O^- CIMS (HNO_3) plus AMS (NO_3) or MC/IC (HNO_3 plus NO_3^-), and for some campaigns, there were large disagreements for some subsets of the data between these two total nitrate measurements. However, as shown in Supplemental Figure 18, this disagreement does not substantially affect the aerosol pH, with slope differences of less than 2%. Though for some campaigns the evaluation plots of gas- and particle-phase nitrate is worse using the MC/IC compared to the CIMS and AMS and led to increased scatter in the aerosol pH (Supplemental Figure 21), it did not impact the average aerosol pH.

CalNex was the only campaign with gas-phase ammonia measurements. This campaign was used to investigate potential biases using the iteration method for ammonia gas for the other 10 campaigns that did not have ammonia measurements. We ran E-AIM similar to other campaigns (without ammonia gas mixing ratios as input) and with total NH_x (ammonia gas plus particle-phase NH_4) (Supplemental Figure 22). In the E-AIM model without ammonia gas input, there is a larger point-to-point scatter for the predicted versus observed ammonia; however, the

model predicted the campaign average ammonia gas-phase concentration within a factor of 2 (Supplemental Figure 22 and 23). On the other hand, the model, on average, predicted the partitioning of the gas- versus particle-phase ammonia and the predicted particle-phase ammonium well (Supplemental Figure 22). Finally, the predicted pH changed by ~0.1 pH unit between the model with and without total ammonia input (Supplemental Figure 24a). The regression between the two cases shows some point-to-point variability (R^2 = 0.78) but still shows a slope near 1 (1.11) (Supplemental Figure 24b). Therefore, these sensitivity analyses suggest that the predicted aerosol pH for the campaigns without ammonia gas-phase measurements are well constrained by the use of total nitrate, similar to prior studies[68].

Supplemental Tables

Supplemental Table 1. ***References for processes represented in Fig. 1****.*

Process	Reference
IEPOX Reaction Probability	Gaston et al.[69]
HO_2 Reaction Probability	Thornton et al.[70]
Iron pH dependent dissolution	Meskhidze et al.[71]
S(IV) Compound and Aqueous Oxidation	Seinfeld and Pandis[27]
Partitioning NH_3/NH_4^+, HNO_3/NO_3^-, HCl/Cl^-	Guo et al.[38]
Aldehyde/Diol Equilibrium (Brown Carbon)	Ackendorf et al.[72]
Organic aerosol phase separation	Losey et al.[73]

Supplemental Table 2. ***Campaigns and subregions used in this study.***

Location	Field Campaign	Coordinates		Time Period	Season
		Longitude (°)	Latitude (°)		
Central Mexico	MILAGRO[74]	−102 – −88	16 – 28	04 March 2006 – 29 March 2006	Spring
Western US & Eastern Pacific	INTEX-B[75]	−141 – −118	37 - 54	17 April 2006 – 15 May 2006	Spring
Canada, Alaska, Greenland	ARCTAS-A[76]	−180 – −37	60 - 90	18 March 2008 – 19 April 2008	Spring
Canada, Greenland	ARCTAS-B[76]	−136 – −37	50 – 87	26 June 2008 – 13 July 2008	Summer
California, USA	CalNex[77]	−124 – −115	33 – 40	20 April 2010 – 22 June 2010	Spring
Central and Eastern USA	DC3[78]	−106 – −78	30 – 43	04 May 2012 – 23 June 2012	Spring
USA	SEAC^{4}RS[79]	−126 – −79	19 – 51	02 August 2013 – 23 Sept 2013	Summer
Eastern USA	WINTER[68,80]	−85 – −67	32 – 43	01 Feb 2015 – 15 March 2015	Winter
South Korea	KORUS-AQ[55,81]	123 – 133	30 – 39	01 May 2016 – 09 June 2016	Spring
ATom >50°	ATom-1 & -2[36]	−150 – 0	>50	29 July 2016 – 23 August 2016; 26 Jan 2017 – 21 Feb 2016	Summer[a] Winter[b]
ATom Pacific 25° - 50°	ATom-1 & -2[36]	−180 – −130	25 – 50	29 July 2016 – 23 August 2016; 26 Jan 2017 – 21 Feb 2016	Summer[a] Winter[b]
ATom Pacific −25° to 25°	ATom-1 & -2[36]	−180 – −130	−25 – 25	29 July 2016 – 23 August 2016; 26 Jan 2017 – 21 Feb 2016	Summer[a] Winter[b]
ATom Pacific −50° to −25°	ATom-1 & -2[36]	−180 – −130	−50 – −25	29 July 2016 – 23 August 2016; 26 Jan 2017 – 21 Feb 2016	Summer[a] Winter[b]
ATom <−50°	ATom-1 & -2[36]	−180 – −30	< −50	29 July 2016 – 23 August 2016; 26 Jan 2017 – 21 Feb 2016	Summer[a] Winter[b]
ATom Atlantic −50° to −25°	ATom-1 & -2[36]	−45 – 0	−50 – −25	29 July 2016 – 23 August 2016; 26 Jan 2017 – 21 Feb 2016	Summer[a] Winter[b]
ATom Atlantic −25° to 25°	ATom-1 & -2[36]	−45 – 0	−25 – 25	29 July 2016 – 23 August 2016; 26 Jan 2017 – 21 Feb 2016	Summer[a] Winter[b]
ATom Atlantic 25° - 50°	ATom-1 & -2[36]	−45 – 0	25 – 50	29 July 2016 – 23 August 2016; 26 Jan 2017 – 21 Feb 2016	Summer[a] Winter[b]

[a]ATom-1 was during boreal summer

[b]ATom-2 was during boreal winter

Supplemental Table 3. ***Instruments used in this study.***

Campaign	NO_3 Measurement	SO_4 and NH_4 Measurement	NH_3 Measurement	HNO_3 Measurement
MILAGRO	HR-AMS[82,83]	HR-AMS[82,83]	N/A	CF_3O-CIMS[84]
INTEX-B	HR-AMS[82,85]	HR-AMS[82,85]	N/A	CF_3O-CIMS[84]
ARCTAS-A	HR-AMS[82,86] MC/IC[87]	HR-AMS[82,86]	N/A	CF_3O-CIMS[84] MC/IC[87]
ARCTAS-B	HR-AMS[82,86] MC/IC[87]	HR-AMS[82,86]	N/A	CF_3O-CIMS[84] MC/IC[87]
CalNex	c-ToF-AMS[88,89]	c-ToF-AMS[88,89]	Acetone-CIMS[90]	SiF_5^--CIMS[91]
DC3	HR-AMS[82] MC/IC[87]	HR-AMS[82]	N/A	CF_3O-CIMS[84] MC/IC[87]
SEAC^{4}RS	HR-AMS[82] MC/IC[87]	HR-AMS[82]	N/A	CF_3O-CIMS[84] MC/IC[87]
WINTER	HR-AMS[80,82]	HR-AMS[80,82]	N/A	I-CIMS[92]
KORUS-AQ	HR-AMS[55,82] MC/IC[87]	HR-AMS[55,82]	N/A	CF_3O-CIMS[84] MC/IC[87]
ATom-1	HR-AMS[20,36,82] MC/IC[87]	HR-AMS[20,36,82]	N/A	CF_3O-CIMS[84] MC/IC[87]
ATom-2	HR-AMS[20,36,82] MC/IC[87]	HR-AMS[20,36,82]	N/A	CF_3O-CIMS[84] MC/IC[87]

Supplemental Table 4. ***Chemical transport models used along with brief information about the models (model year, output, etc.).*** *For models that calculated pH on-line, ISORROPIA v2 was used.*

Model	AeroCom-II or Post-AeroCom-II	pH Calculated on-line/off-line	Model Year	Reference
CCSM4	AeroCom-II	off-line	01/2006 - 12/2006	Tsigaridis et al.[93]
GISS-MATRIX	AeroCom-II	off-line	01/2006 - 12/2006	Tsigaridis et al.[93]
GISS-ModelE	AeroCom-II	off-line	01/2006 - 12/2006	Tsigaridis et al.[93]
TM4-ECPL-F	AeroCom-II	N/A	01/2006 - 12/2006	Tsigaridis et al.[93]
GEOS-Chem v10	Post-AeroCom-II	on-line	08/2013 - 07/2014	Marais et al.[94]
GEOS-Chem v12	Post-AeroCom-II	on-line	07/2013 - 06/2014	Jo et al.[95]
GEOS-5	Post-AeroCom-II	off-line	03/2016 - 02/2017	Bian et al.[96]
GEOS-Chem TOMAS	Post-AeroCom-II	off-line	01/2016 - 12/2016	Kodros and Pierce[97]
AM4.1	Post-AeroCom-II	on-line	01/2007 - 12/2007	Horowitz et al.[98]

Supplemental Table 5. ***Slopes and intercepts for ammonium balance ($((NH_4/18)/((2\times SO_4/96)+(NO_3/62))$) versus log_{10}(Inorganic PM_1) for observations and models by pressure levels.***

Data	Pressure Level	Slope	Intercept	R^2
Ambient Observations	Surface to 800 hPa	0.37±0.07[a]	0.60±0.05[c]	0.57
	800 to 400 hPa	0.53±0.07[a]	0.76±0.04[c]	0.74
	400 to 250 hPa	0.45±0.07[a]	0.57±0.07[c]	0.66
CCSM4	Surface to 800 hPa	–0.04±0.09	0.86±0.05	0.01
	800 to 400 hPa	–0.20±0.20	0.83±0.16	0.04
	400 to 250 hPa	0.46±0.28	1.49±0.40	0.10
GISS-MATRIX	Surface to 800 hPa	–0.08±0.11	0.65±0.05	0.02
	800 to 400 hPa	0.27±0.15[b]	0.79±0.11[d]	0.12
	400 to 250 hPa	0.83±0.15[b]	1.58±0.20	0.59
GISS-ModelE	Surface to 800 hPa	0.08±0.12	0.90±0.06	0.02
	800 to 400 hPa	0.60±0.20[b]	1.24±0.14	0.29
	400 to 250 hPa	1.26±0.25	2.27±0.31	0.54
TM4-ECPL-F	Surface to 800 hPa	0.40±0.05[b]	0.84±0.04	0.70
	800 to 400 hPa	0.35±0.11[b]	1.06±0.12	0.32
	400 to 250 hPa	0.84±0.14	1.54±0.22	0.59
GEOS-Chem v10	Surface to 800 hPa	0.31±0.08[b]	0.73±0.04	0.40
	800 to 400 hPa	0.36±0.13[b]	0.79±0.08[d]	0.25
	400 to 250 hPa	0.18±0.16[b]	0.60±0.13	0.06
GEOS-Chem v12, Default	Surface to 800 hPa	0.42±0.08[b]	0.57±0.04[d]	0.52
	800 to 400 hPa	0.43±0.10[b]	0.66±0.05[d]	0.44
	400 to 250 hPa	0.46±0.11[b]	0.64±0.07[d]	0.43
GEOS-Chem TOMAS	Surface to 800 hPa	0.23±0.09[b]	0.71±0.04[d]	0.22
	800 to 400 hPa	0.28±0.12[b]	0.69±0.07[d]	0.19
	400 to 250 hPa	0.31±0.12[b]	0.65±0.08[d]	0.22
GEOS-5	Surface to 800 hPa	0.10±0.07	0.48±0.03	0.10
	800 to 400 hPa	0.35±0.09[b]	0.66±0.07[d]	0.41
	400 to 250 hPa	0.63±0.12[b]	1.02±0.11	0.57
AM4.1	Surface to 800 hPa	0.28±0.07[b]	0.59±0.03[d]	0.41
	800 to 400 hPa	0.46±0.10[b]	0.75±0.04[d]	0.48
	400 to 250 hPa	0.65±0.09[b]	0.97±0.07	0.68

[a]The observational trends at all three pressure levels are statistically similar at 95% confidence interval.
[b]The trend in model is statistically similar to the trend in observation at 95% confidence interval.
[c]The observational y-intercept at all three pressure levels are statistically similar at 95% confidence interval.
[d]The y-intercept from model results is statistically similar to the y-intercept from the observations at 95% confidence interval. Only compared with slopes that were statistically similar ([b]).
[e] The y-intercept from model results is statistically similar to the y-intercept from the observations at 97.5% confidence interval. Only compared with slopes that were statistically similar ([b]).

Supplemental Table 6. ***Slopes and intercepts for aerosol pH versus log_{10}(Inorganic PM_1) for observations and models by pressure levels.*** *For TM4-ECPL-F, there are not enough outputs to calculate aerosol pH.*

Data	Pressure Level	Slope	Intercept	R^2
Ambient Observations	Surface to 800 hPa	0.97±0.18[a]	0.36±0.12[c]	0.55
	800 to 400 hPa	1.38±0.15[a]	0.60±0.11[c]	0.64
	400 to 250 hPa	1.35±0.24[a]	0.54±0.21[c]	0.72
CCSM4	Surface to 800 hPa	0.00±0.16	0.63±0.09	0.00
	800 to 400 hPa	–0.33±0.26	1.51±0.18	0.08
	400 to 250 hPa	–0.58±0.19	1.56±0.25	0.34
GISS-MATRIX	Surface to 800 hPa	0.35±0.38[b]	0.69±0.15[d]	0.04
	800 to 400 hPa	0.52±0.39[b]	1.30±0.28	0.09
	400 to 250 hPa	1.45±0.43[b]	2.32±0.58	0.38
GISS-ModelE	Surface to 800 hPa	0.07±0.23	1.68±0.11	0.00
	800 to 400 hPa	1.52±0.63[b]	3.39±0.47	0.20
	400 to 250 hPa	2.08±0.76	4.12±0.95	0.24
TM4-ECPL-F	Surface to 800 hPa	–	–	–
	800 to 400 hPa	–	–	–
	400 to 250 hPa	–	–	–
GEOS-Chem v10	Surface to 800 hPa	–0.72±0.36	1.70±0.17	0.15
	800 to 400 hPa	0.90±0.69[b]	1.01±0.43[d]	0.07
	400 to 250 hPa	3.03±0.90	2.52±0.75	0.33
GEOS-Chem v12, Default	Surface to 800 hPa	–0.39±0.31	1.16±0.14	0.06
	800 to 400 hPa	0.67±0.36[b]	0.14±0.16	0.13
	400 to 250 hPa	1.44±0.32[b]	0.30±0.20	0.48
GEOS-Chem TOMAS	Surface to 800 hPa	0.96±0.26[b]	0.58±0.12[d]	0.37
	800 to 400 hPa	1.08±0.37[b]	0.67±0.22[d]	0.28
	400 to 250 hPa	1.41±0.36[b]	0.74±0.23[d]	0.40
GEOS-5	Surface to 800 hPa	0.90±0.22[b]	0.49±0.11[d]	0.42
	800 to 400 hPa	1.68±0.24[b]	1.47±0.19	0.68
	400 to 250 hPa	1.61±0.49[b]	1.64±0.48	0.32
AM4.1	Surface to 800 hPa	0.84±0.19[b]	0.13±0.09[d]	0.45
	800 to 400 hPa	1.63±0.29[b]	0.44±0.12[d]	0.58
	400 to 250 hPa	2.06±0.33	0.84±0.23	0.63

[a]The observational trends at all three pressure levels are statistically similar at 95% confidence interval.
[b]The trend in model is statistically similar to the trend in observation at 95% confidence interval.
[c]The observational y-intercept at all three pressure levels are statistically similar at 95% confidence interval.
[d]The y-intercept from model results is statistically similar to the y-intercept from the observations at 95% confidence interval. Only compared with slopes that were statistically similar ([b]).

Supplemental Table 7. ***Description of GEOS-Chem v12 sensitivity runs conducted for Fig. 7.***

Model	**Inorganic Phase State Considered**	**Oceanic NH_x Emissions**	**Reduced/ Increased NH_3 Henry's Constant**	**Reduced Terrestrial NH_3 Emissions**
Base	No	GEIA	N/A	No
Update HGF	Yes	GEIA	N/A	No
Update HGF and Decreased NH_x H	Yes	GEIA	Reduced	No
Update HGF Reduced NH_x Ocean Emiss.	Yes	Paulot et al.[4]	N/A	No
Update HGF Reduced NH_x Ocean & Cont. Emiss.	Yes	Paulot et al.[4]	N/A	Yes
Update HGF Reduced NH_x Emissions and Increased NH_x H	Yes	Paulot et al.[4]	Increased	No

Supplemental Table 8. ***Evaluation of reduced nitrogen organic compounds in aerosol from different studies.*** *Unless otherwise noted, the values reported are the mean from the study.*

Reference	Amines ($ng\ m^{-3}$)	Ammonium ($ng\ m^{-3}$)	Amines: Ammonium[a]	Location	Dates Sampled
Müller et al.[99]	Mean = 0.57 Median = 0.53	Mean = 80 Median = 63	Mean = 0.007 Median = 0.008	16.86°N, 24.87°W & 17.59°N, 24.28°W	May 2007 - June 2008
van Pinxteren et al.[100]	13	690	0.02	16°N, 24°W to 5°S, 4°E	22 June - 21 July, 2011
Frossard et al.[101]	30	N/A	N/A	See Ref. 132; overview of multiple studies	See Ref. 132; overview of multiple studies
Sorooshian et al.[60]	22	N/A	N/A	37.0°N, 123.5°W to 35.5°N, 122.0°W & 38.10°N, 122.96°W	June 2005 - July 2007
Youn et al.[102]	14	240	0.06	32.23°N, 110.95°W	July 2012 - June 2013
Gibb et al.[103]	5	44	0.11	20°N, 57°E to 7°N, 67°E	August - December 1994
Facchini et al.[104]	8	N/A	N/A	53°N, 10°W	11 June - 6 July, 2006
Huang et al.[105,b]	Mean = 11 Median = 7	Mean = 190 Median = 140	Mean = 0.06 Median = 0.05	53.55°N, 8.58°E to 33.92°S, 18.42°E or 53.17°N, 70.93°W	April 2011 - November 2012

[a]The ratio is mass concentration ratio, as the amines are a mixture of compounds. Thus, the ratio should be smaller for the molar ratio, once the amines are converted to equivalent ammonium molar concentration.

[b]Aerosol amines were measured by an Aerosol Mass Spectrometer. A large fraction of the aerosol identified as marine nitrogen-containing OA was assigned to non-nitrogen-containing fragments (82%, with a large oxygen content) versus nitrogen-containing fragments (18%). Therefore, the amines mass concentration was determined by multiplying the entire marine nitrogen-containing OA by the nitrogen fragment fraction of the OA.

Supplemental Figures

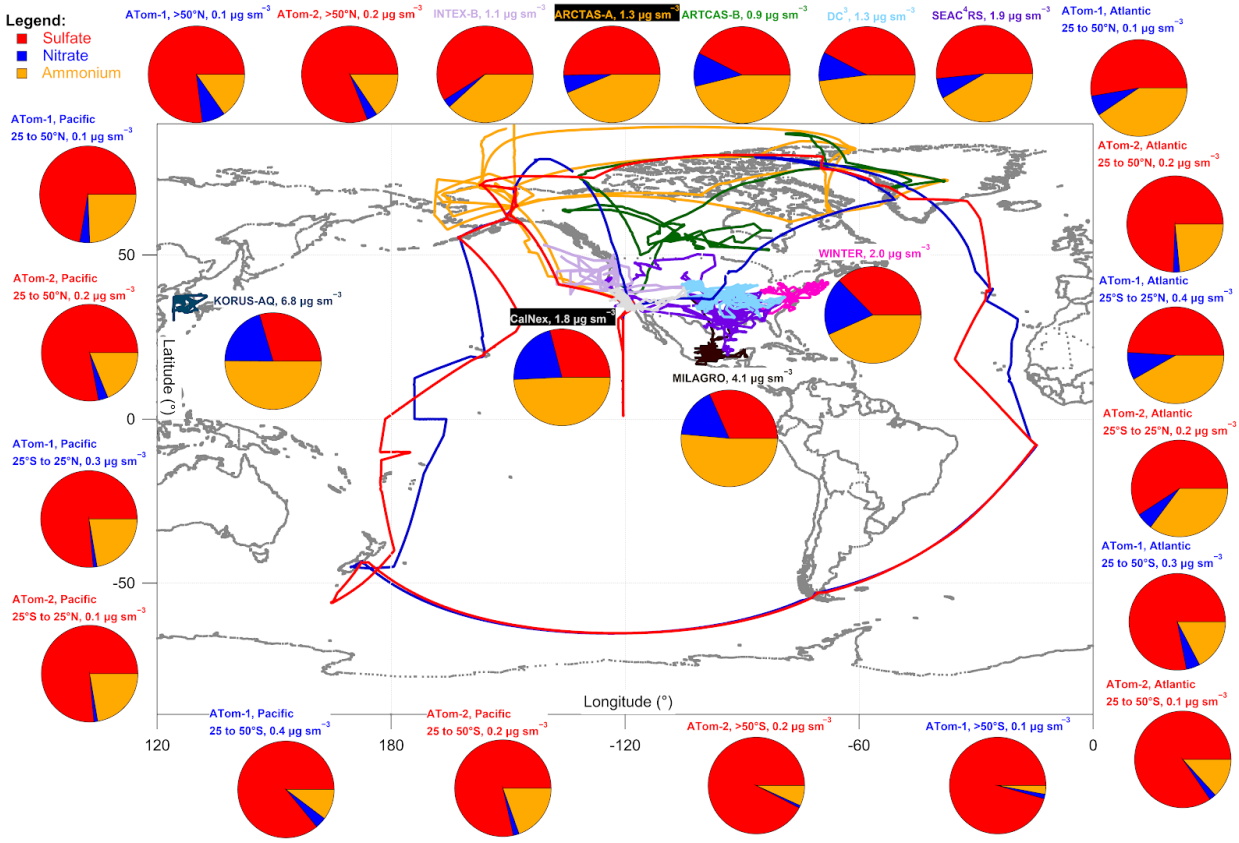

Supplemental Figure 1. ***Map of flight campaigns along with average aerosol molar composition for each campaign.*** *Flight tracks and average inorganic aerosol composition, in molar charge equivalents (NH_4/18 (orange), NO_3/62 (blue), and 2×SO_4/96 (red)), for each campaign and different oceanic locations for ATom-1 and -2 (Supplemental Table 2). The average inorganic mass concentrations are listed above each pie chart, where sm^{-3} is standard meters cubed at constant temperature (273.15 K) and pressure (1013 hPa) (STP).*

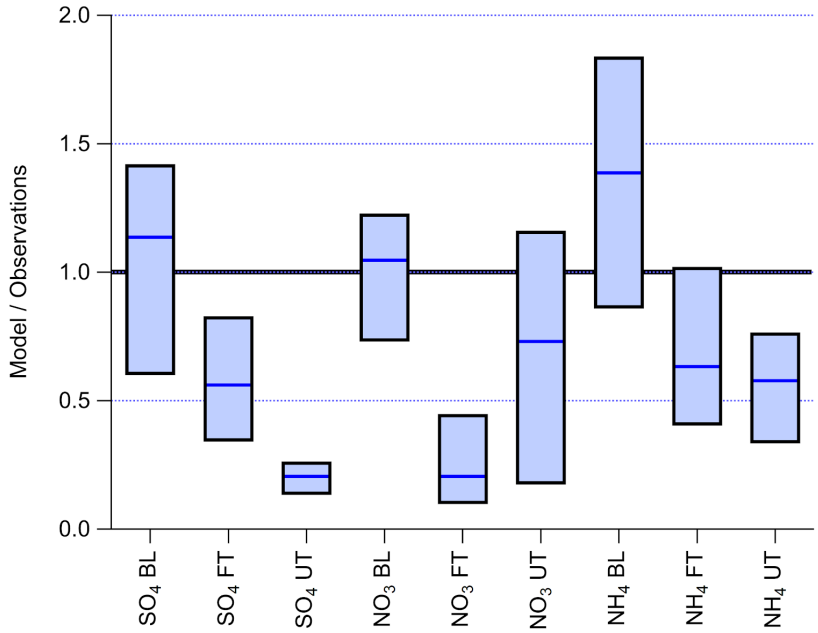

413

414 *Supplemental Figure 2.* ***Comparison of model to observed aerosol concentration by species and***
415 ***altitude.*** *Same as* Fig. 2. *Box plot for the ratios between AeroCom-II modeled and observed*
416 *sulfate (SO_4), nitrate (NO_3), and ammonium (NH_4) for boundary layer (BL, surface to 800 hPa),*
417 *free troposphere (FT, 800 to 400 hPa), and upper troposphere (UT, 400 to 250 hPa) for all*
418 *campaigns not in urban regions (i.e., not CalNex, KORUS-AQ, MILAGRO, and WINTER)*
419 *evaluated here and for AeroCom-II CTMs (CCSM4, GISS-MATRIX, GISS-ModelE, and*
420 *TM4-ECPL-F). The blue horizontal line is the median ratio of the model-to-observations*
421 *ensemble, and the boxes are the 25th and 75th percentiles. For data used here, see the SI File.*

422

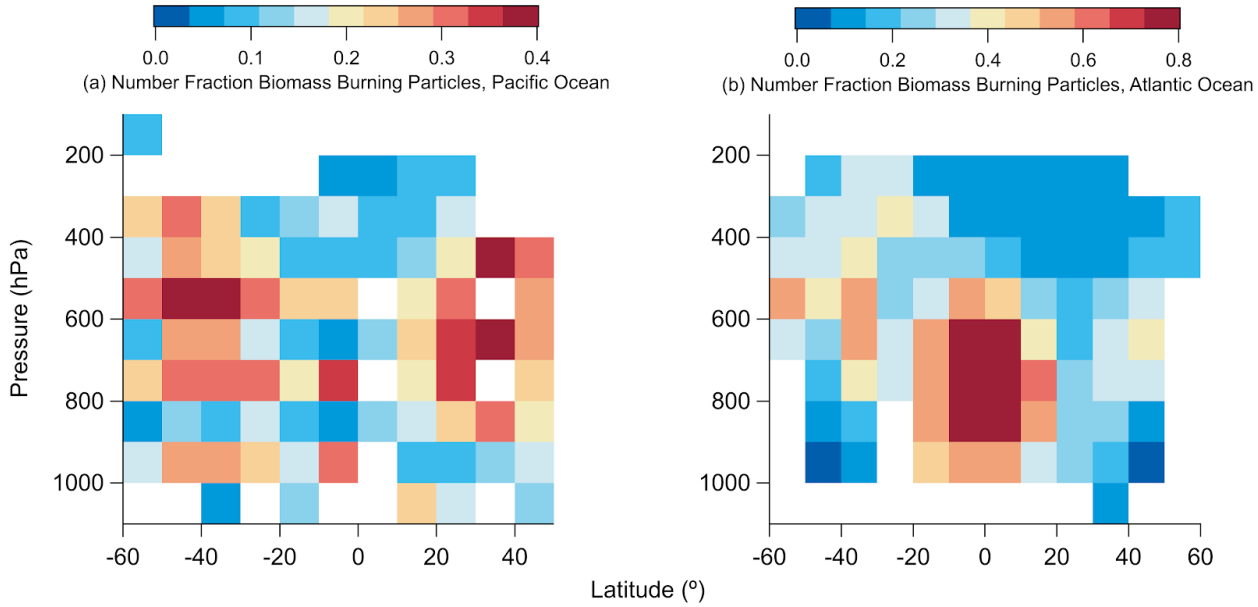

423 *Supplemental Figure 3.* ***Curtain plot of biomass burning marker for Pacific and Atlantic***
424 ***Ocean.*** *Curtain plot of number fraction of aerosol measured as biomass burning, from the NOAA*
425 *single particle mass spectrometer (PALMS)[30], for ATom-1 and -2, over the Pacific (a) and*
426 *Atlantic (b) oceans.*
427

428

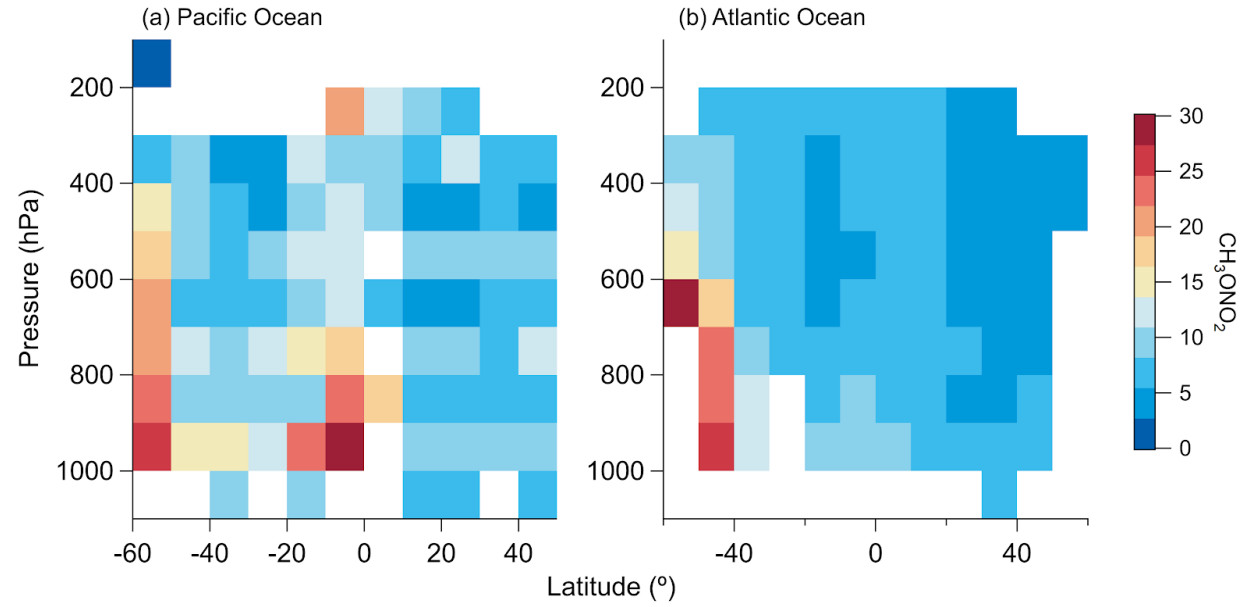

429 *Supplemental Figure 4.* ***Curtain plot of methyl nitrate for Pacific and Atlantic Ocean.*** *Curtain*
430 *plot of methyl nitrate (CH_3ONO_2) measured by University of California, Irvine, whole air*
431 *sampler[106] for ATom-1 and -2, over the Pacific (a) and Atlantic (b) oceans.*

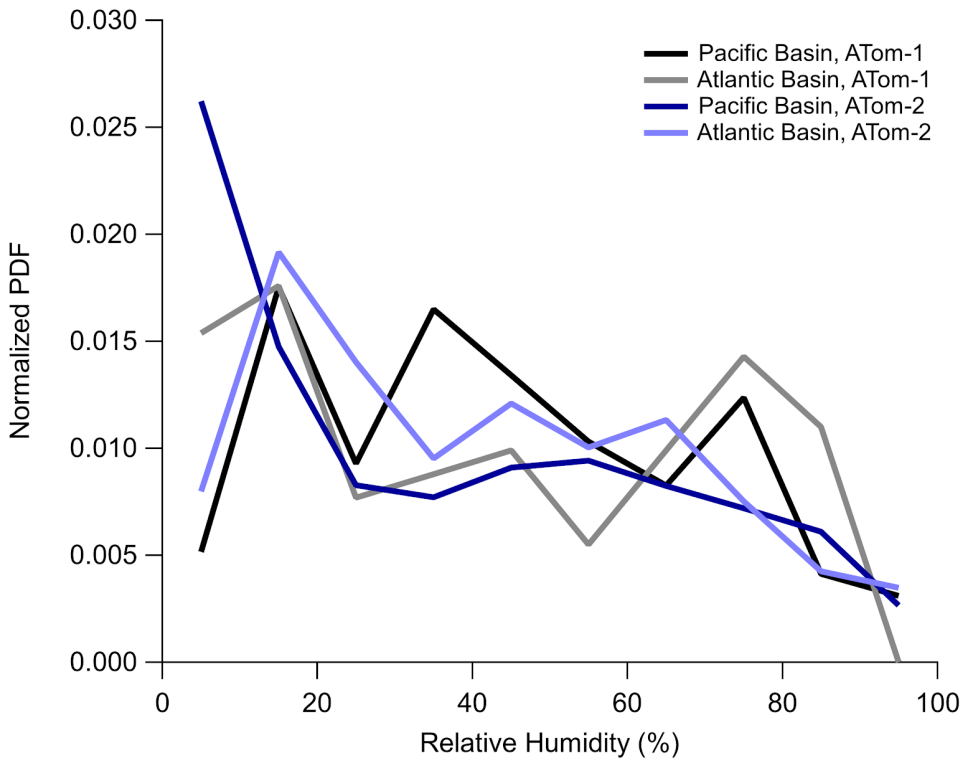

Supplemental Figure 5. ***Probability distribution function of relative humidity for remote oceanic basins.*** *Normalized probability distribution function (PDF) of the relative humidities for the Pacific and Atlantic Basins during ATom-1 and -2. Black is Pacific Basin for ATom-1, grey is Atlantic Basin for ATom-1, dark blue is Pacific Basin for ATom-1, and light blue is Atlantic Basin for ATom-1.*

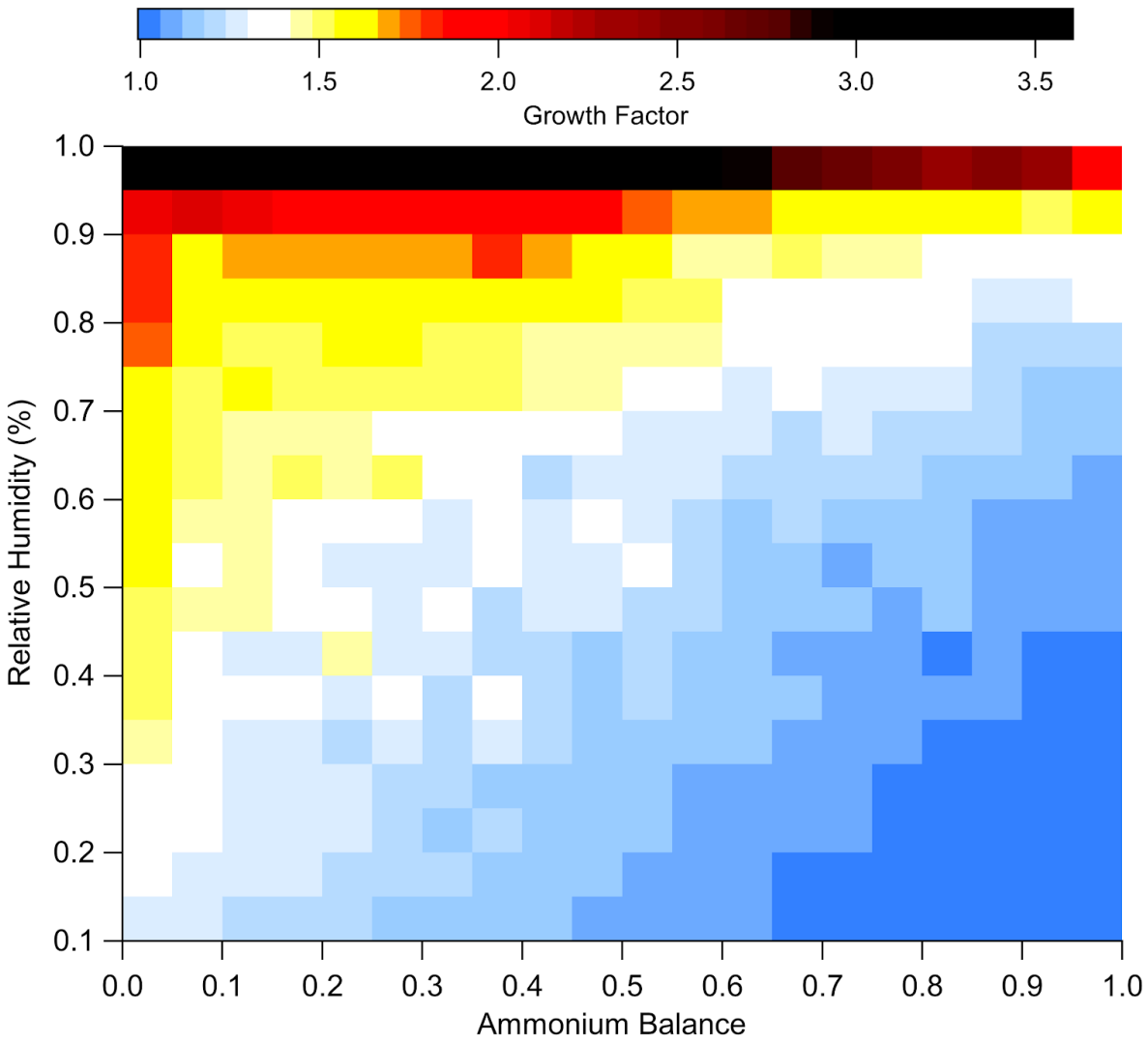

Supplemental Figure 6. ***Behavior of observationally constrained HGF as a function of relative humidity and ammonium balance.*** *Predicted hygroscopic growth factor (HGF) for measured ammonium, nitrate, and sulfate, averaged across campaigns analyzed here (Supplemental Table 2), as a function of relative humidity (left) and ammonium balance (nNH_4 / ($2 \times nSO_4$ + nNO_3)). See Section S2 on details pertaining to the calculation of growth factor. Briefly, HGF was calculated for all data observed (1-minute data) and then binned the calculated HGF as a function of RH and* NH_{4_Bal}.

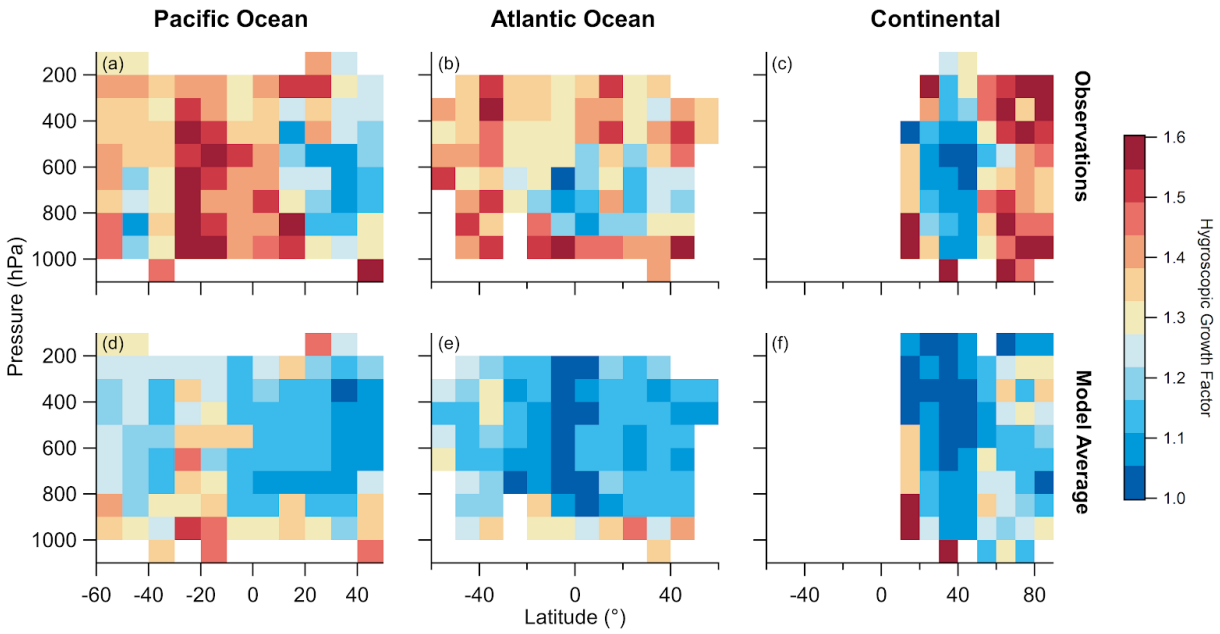

446

447 *Supplemental Figure 7.* ***Curtain plot of observationally constrained and modeled predicted***
448 ***HGF.*** *Curtain plot of the calculated hygroscopic growth factor for the average (a-c)*
449 *observations and (d-f) CTMs over the Pacific and Atlantic basins (ATom-1 and -2) and other*
450 *campaigns (Continental). See Section S2 on details pertaining to the calculation of the growth*
451 *factor. The HGF shown in Supplemental Figure 6 for the CTMs was calculated by using the*
452 *average RH and* NH_{4_Bal} *to estimate the HGF from the look-up table (Supplemental Figure 5).*

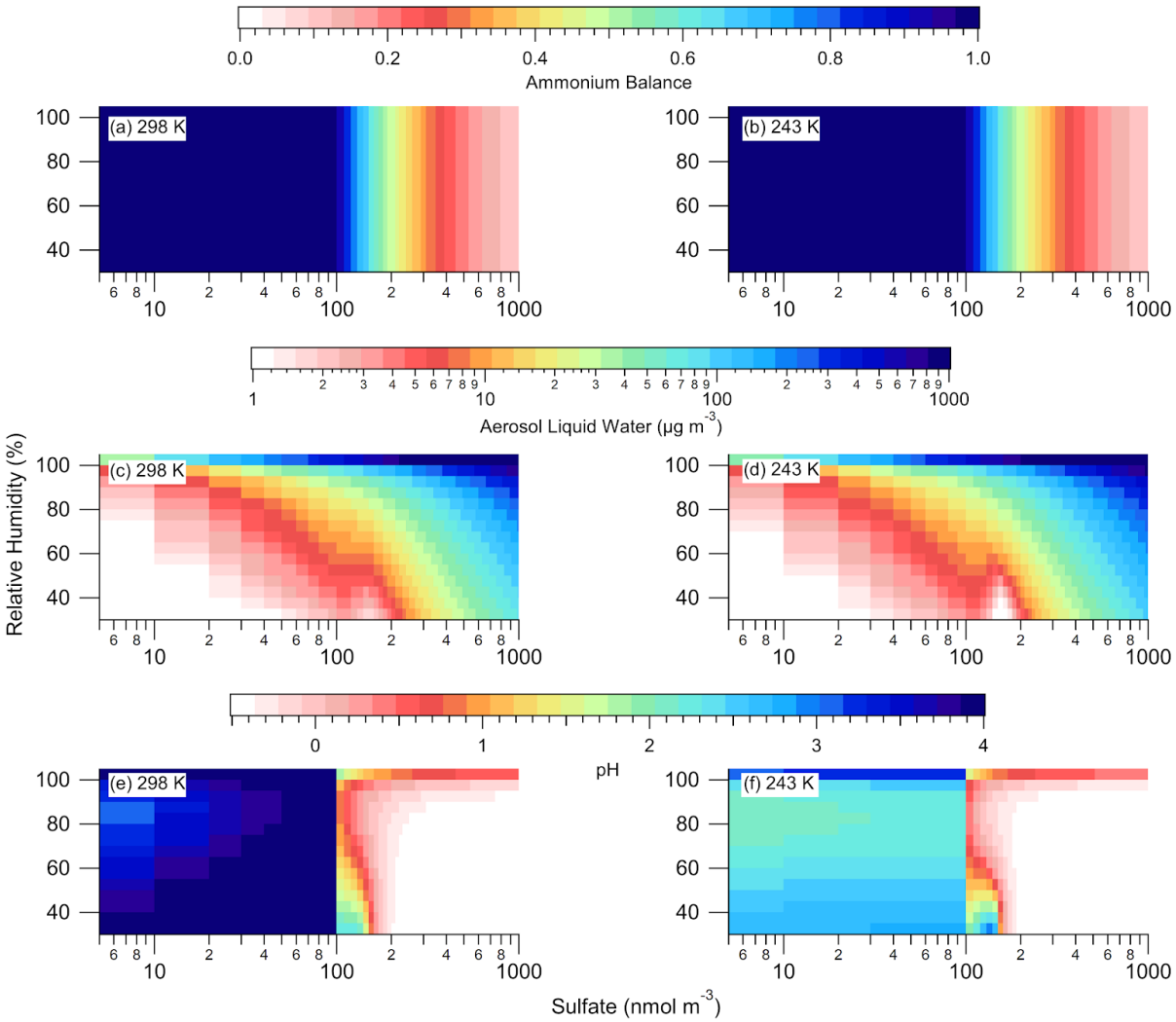

453

454 *Supplemental Figure 8.* ***Predicted behavior of aerosol properties using a box model.*** *Results*
455 *from a box model calculation for aerosol pH using E-AIM, where total ammonium ($NH_{3,g}$ +*
456 *$NH_4^+{}_{,p}$) remained constant at 200 nmol m^{-3}, sulfate varied between 5 to 1000 nmol m^{-3}, relative*
457 *humidity varied between 30 to 95%, and temperature varied between 298 K ((a), (c), and (e))*
458 *and 243 K ((b), (d), and (f)).*

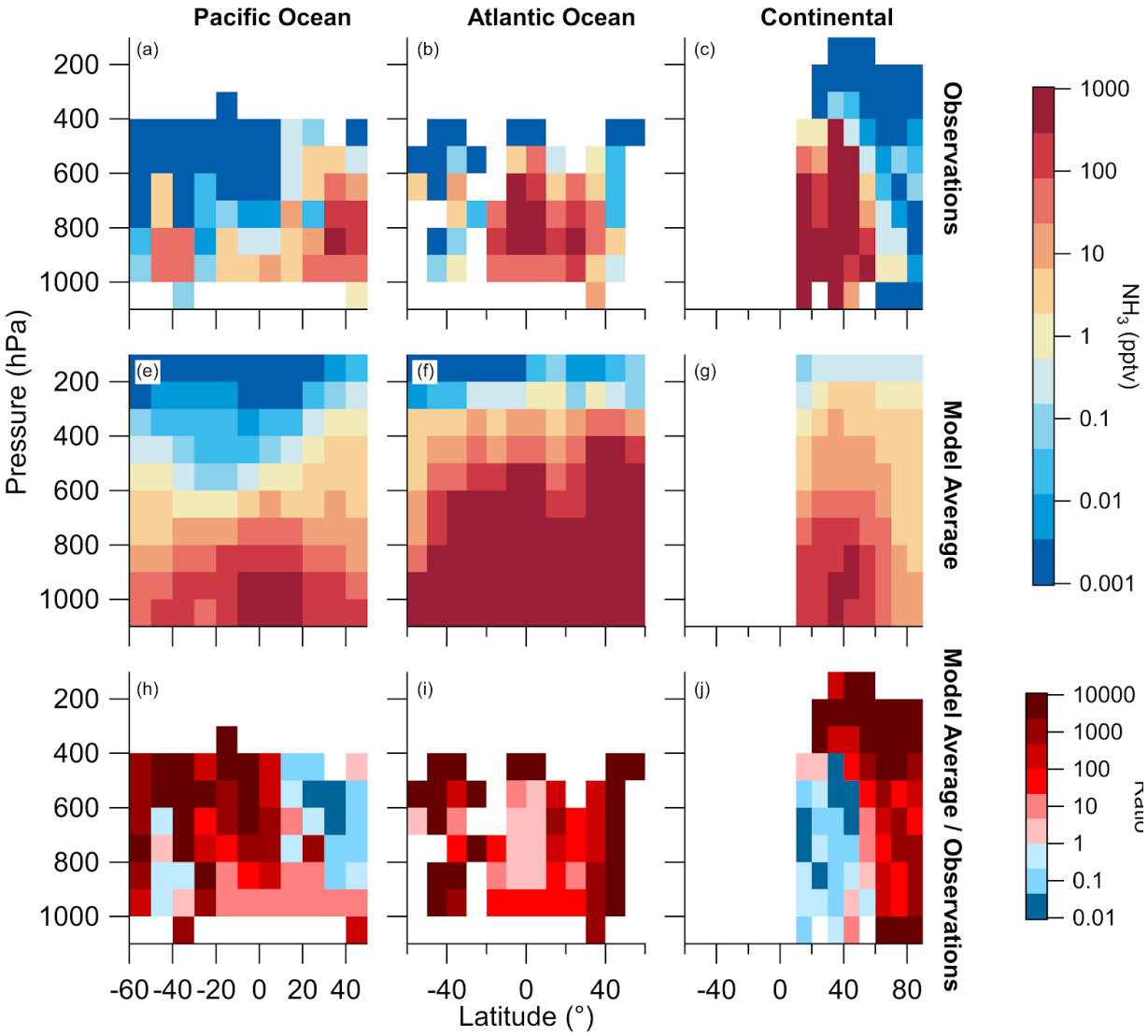

459

460 *Supplemental Figure 9.* ***Curtain plot of observationally constrained and CTM predicted***
461 ***ammonia.*** *Curtain plot of observationally constrained ammonia from E-AIM (a-c), average*
462 *CTMs ammonia (d-f), and ratio of CTMs-to-observations for Pacific Ocean (g), Atlantic Ocean*
463 *(h) and Continental regions (i), as defined in Supplemental Table 2. The models that had*
464 *ammonia as output were used in the curtain plots and include GEOS-Chem v10, GEOS-Chem*
465 *v12, GEOS-Chem TOMAS, GEOS-5, and AM4.1 (Supplemental Table 4).*

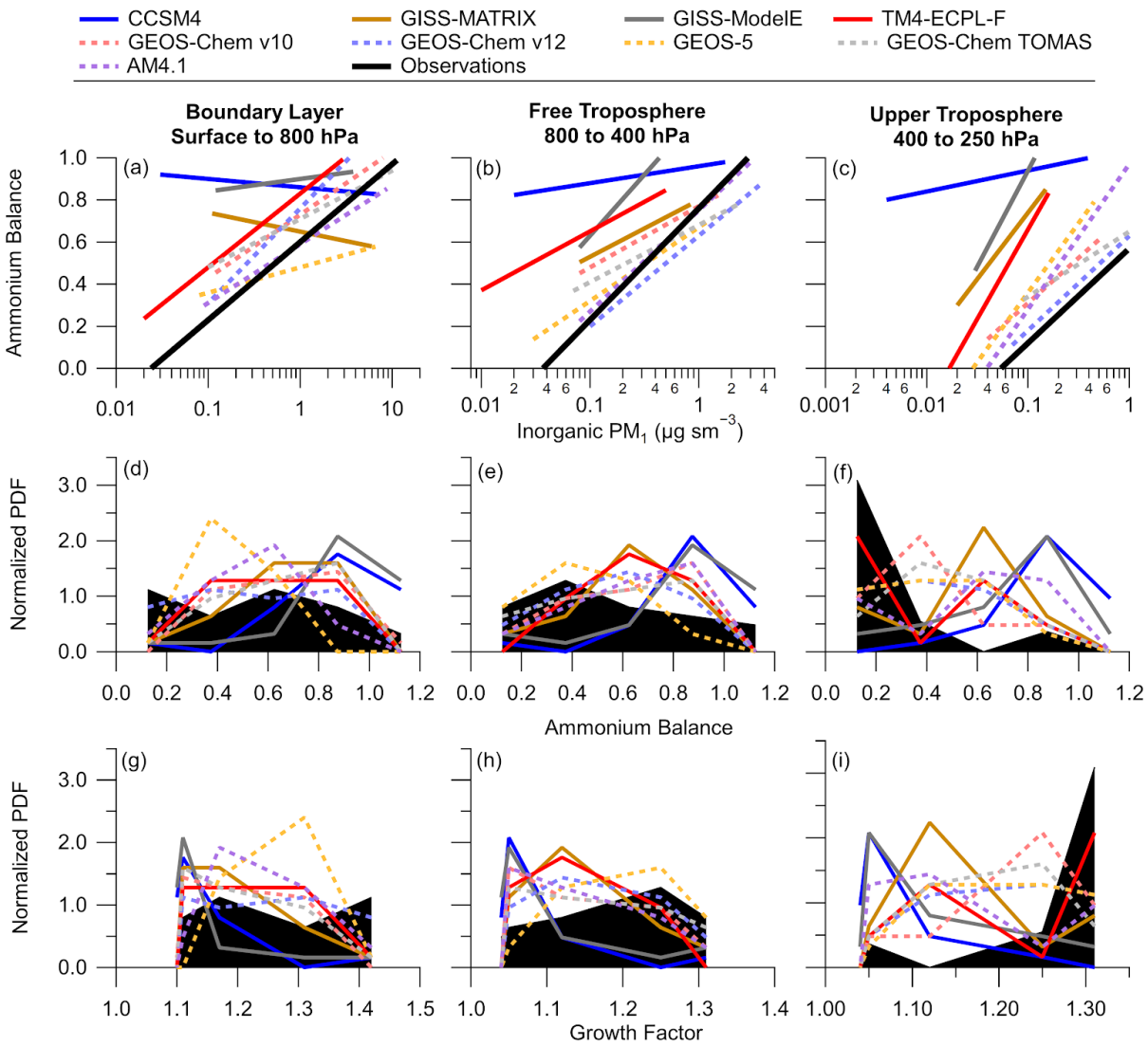

466

467 *Supplemental Figure 10.* ***Comparison of slopes and probability distribution functions for all***
468 ***models and observations.*** *Full results for Fig. 5. (a–c) Comparison of* NH_{4_Bal} *versus*
469 log_{10}*(inorganic* PM_1*) slopes from observations (black) and models (Supplemental Table 5 and*
470 *Supplemental Table 6). (d–f) Normalized probability distribution function (PDF) of* NH_{4_Bal} *for*
471 *observations (solid black) and models. (g–i) Normalized PDF of estimated HGF for observations*
472 *(solid black) and models, using the values from Supplemental Figure 5, and average values RH*
473 *from observations (~50%, ~35%, and ~35% for BL, FT,and UT, respectively). For all figures, the*
474 *AeroCom-II models are solid and the post-AeroCom-II models are dashed. Blue solid is CCSM4,*
475 *gold solid is GISS-MATRIX, grey solid is GISS-ModelE, red solid is TM4-ECPL-F, light red*
476 *dashed is GEOS-Chem v10, light blue dashed is GEOS-Chem v12, orange dashed is GEOS-5,*
477 *grey dashed is GEOS-Chem TOMAS, purple dashed is AM4.1, and black solid is observations.*

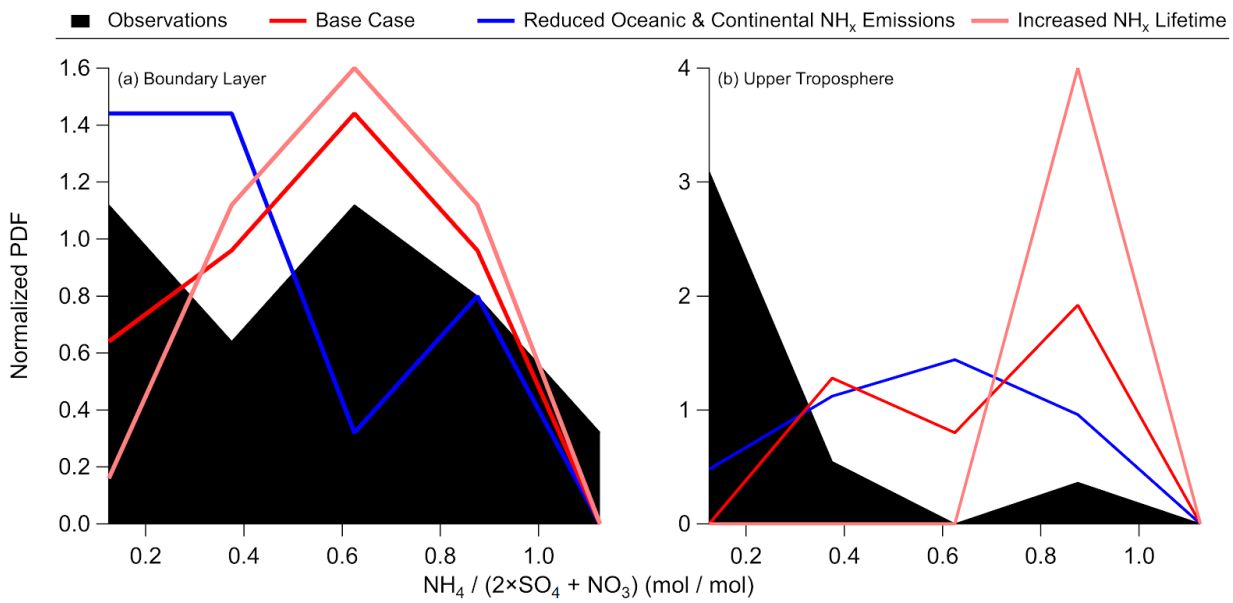

Supplemental Figure 11. ***Probability distribution function results from observations and various GEOS-Chem cases studies, where various factors impacting ammonium were explored.*** *Similar to Supplemental Figure 10d-f, but normalized probability distribution function of ammonium balance from GEOS-Chem v12 total ammonia sensitivity cases (*Supplemental *Table 7) for (a) Boundary Layer (surface to 800 hPa) and (b) Upper Troposphere (400 to 250 hPa). Black is observations, red is base case, blue is reduced oceanic and continental NH_x emissions, and light red is increased NH_x lifetime.*

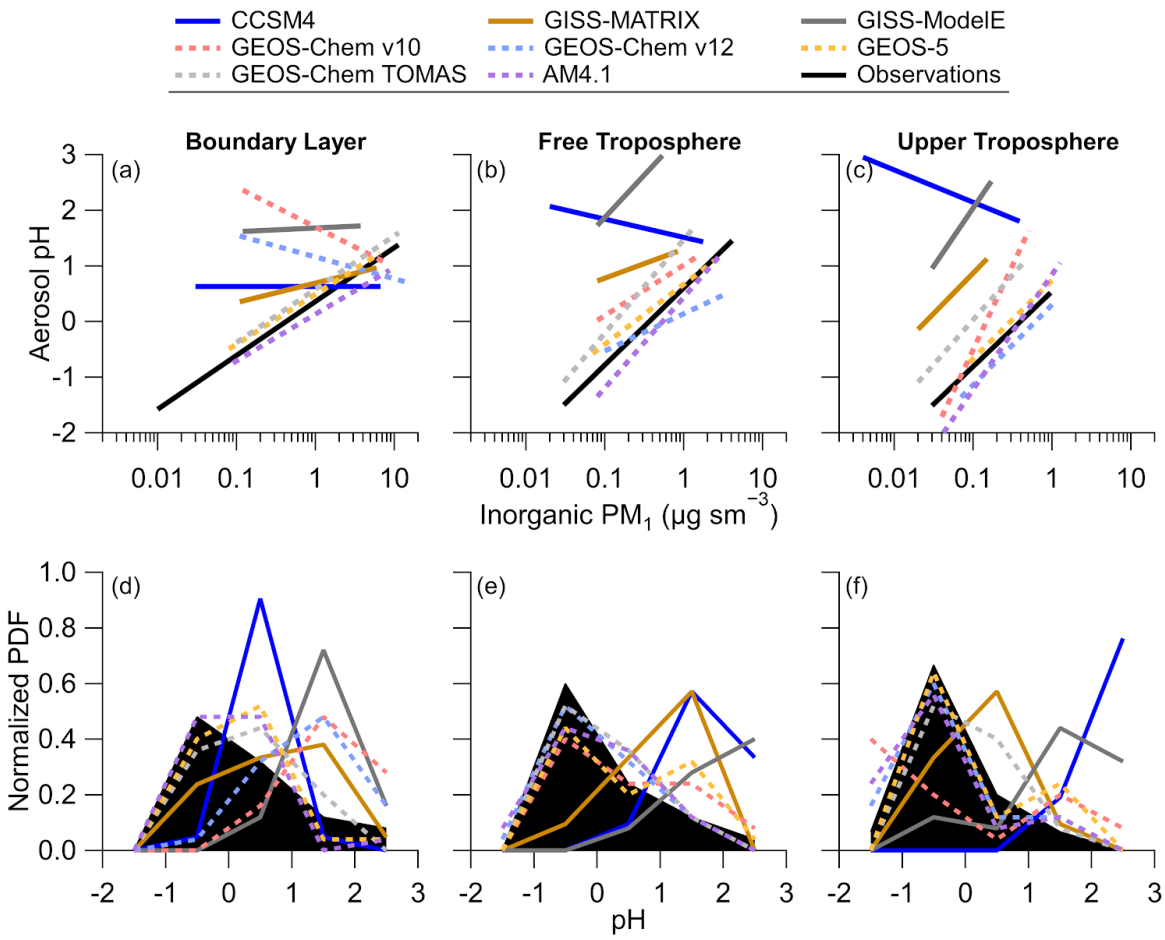

Supplemental Figure 12. ***Comparison of slopes and probability distribution functions for all models and observations.*** *Full results for Fig. 6. (a–c) Comparison of pH versus log10(inorganic PM1) slopes from observations (black) and models (Supplemental Table 5 and Supplemental Table 6). (d–f) Normalized PDF of pH for observations (solid black) and models. BL = surface-800 hPa, FT = 800-400 hPa, and UT = 400-250 hPa. For all figures, the AeroCom-II models are solid and the post-AeroCom-II models are dashed. Blue solid is CCSM4, gold solid is GISS-MATRIX, grey solid is GISS-ModelE, light red dashed is GEOS-Chem v10, light blue dashed is GEOS-Chem v12, orange dashed is GEOS-5, grey dashed is GEOS-Chem TOMAS, purple dashed is AM4.1, and black solid is observations.*

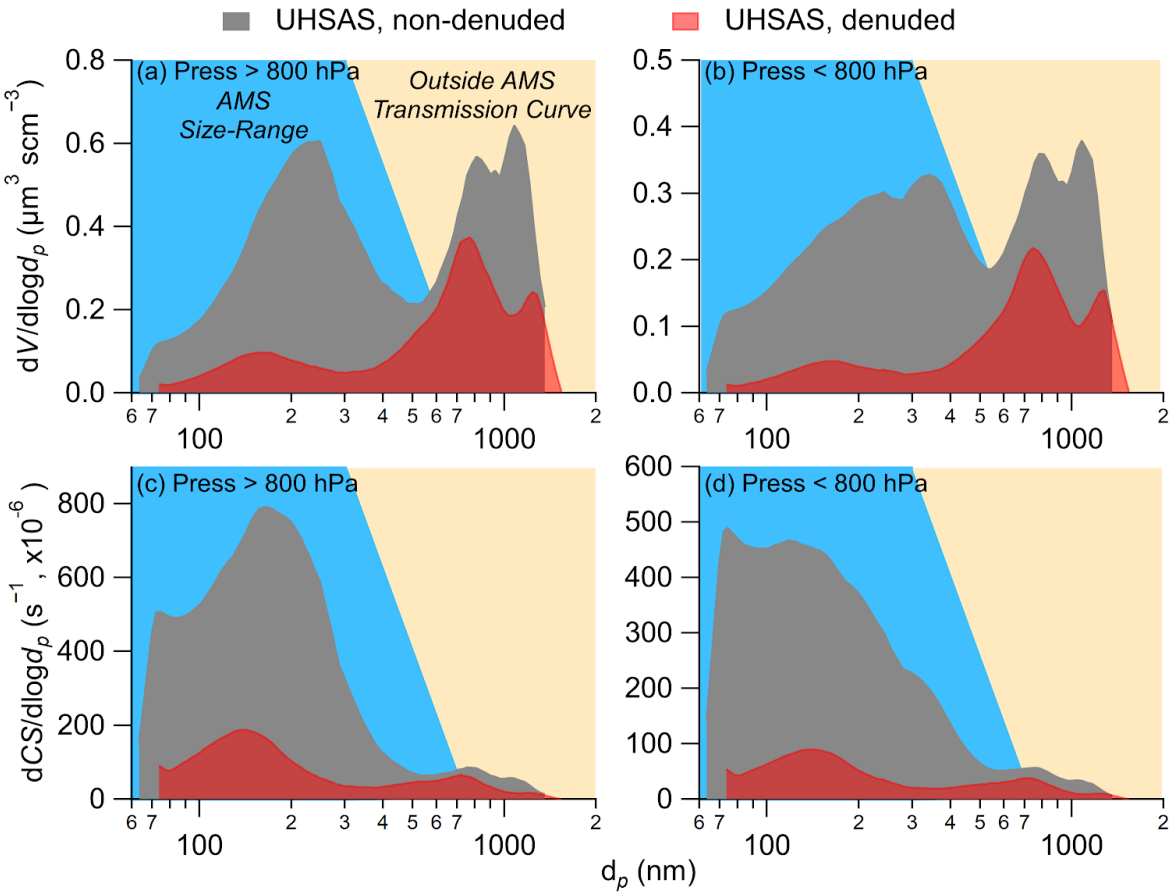

496

497 *Supplemental Figure 13* ***Investigation into the influence of non-volatile cations in the volume***
498 ***distribution and condensational sink during ATom.*** *Average volume distribution (a,b) and*
499 *condensational sink distribution (c,d) of measured total aerosol (UHSAS, non-denuded, grey)*
500 *and nonvolatile/refractory aerosol (UHSAS, denuded, red) during ATom-2 for air sampled within*
501 *marine boundary layer (pressure > 800 hPa, (a) & (c)) and in free/upper troposphere (pressure*
502 *< 800 hPa, (b) & (d)). The transmission curve (defining diameters of aerosol observed by AMS),*
503 *from Guo et al.*[20]*, is shown in blue, and the aerosol not observed by AMS is shown in tan.*

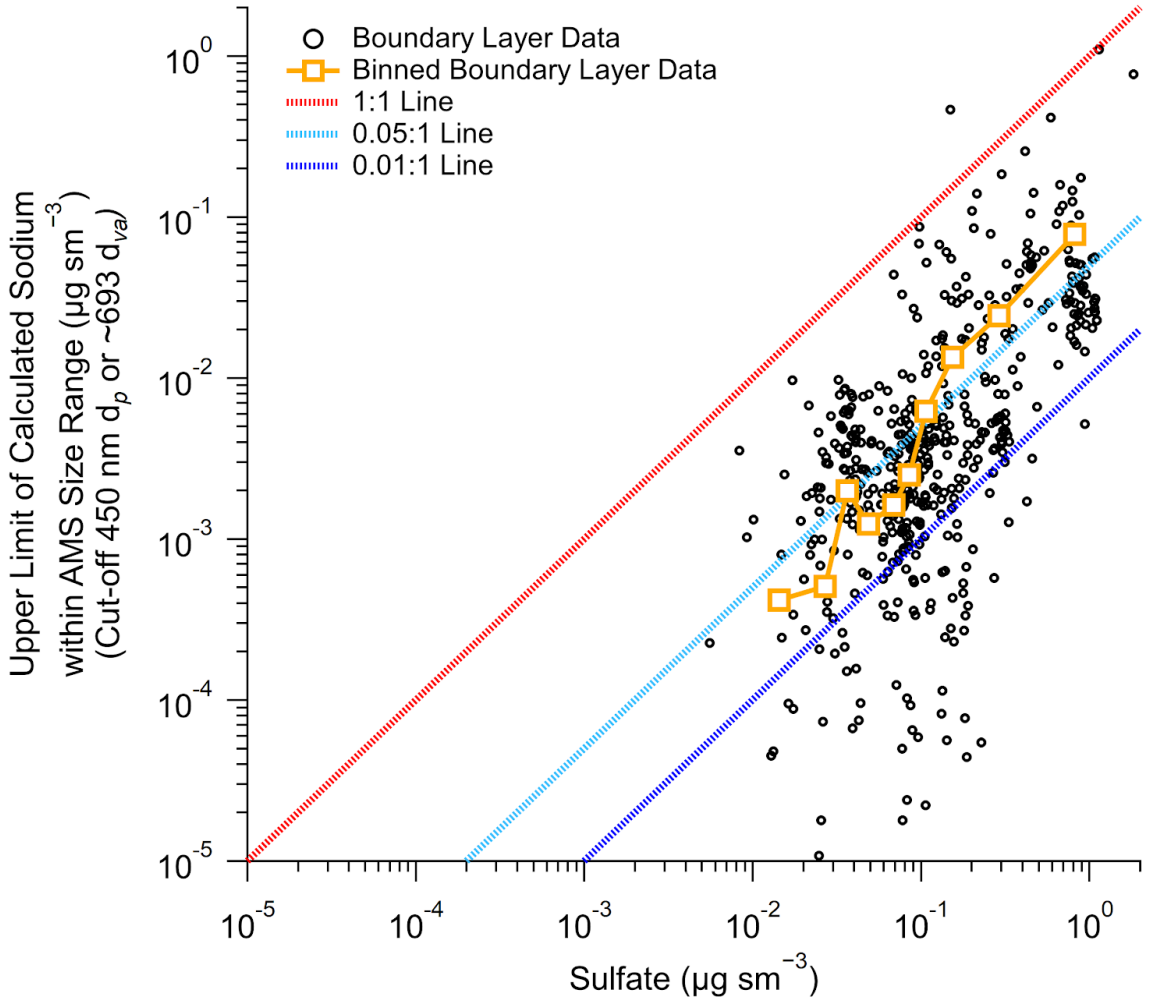

Supplemental Figure 14. ***Comparison of predicted submicron sodium with sulfate measured by the AMS during ATom.*** *Scatter plot of calculated sodium mass concentration (see Sect. S4.4 for details on calculation), for geometric diameters up to 450 nm (the 50% diameter cut-off for AMS[20]) versus measured sulfate, in the boundary layer (surface to 800 hPa) during ATom-2. Black circles are all data in the boundary layer, orange square is the binned data, red dashed is the 1:1 line, light blue is 0.05:1 line, and blue dashed is 0.01:1 line.*

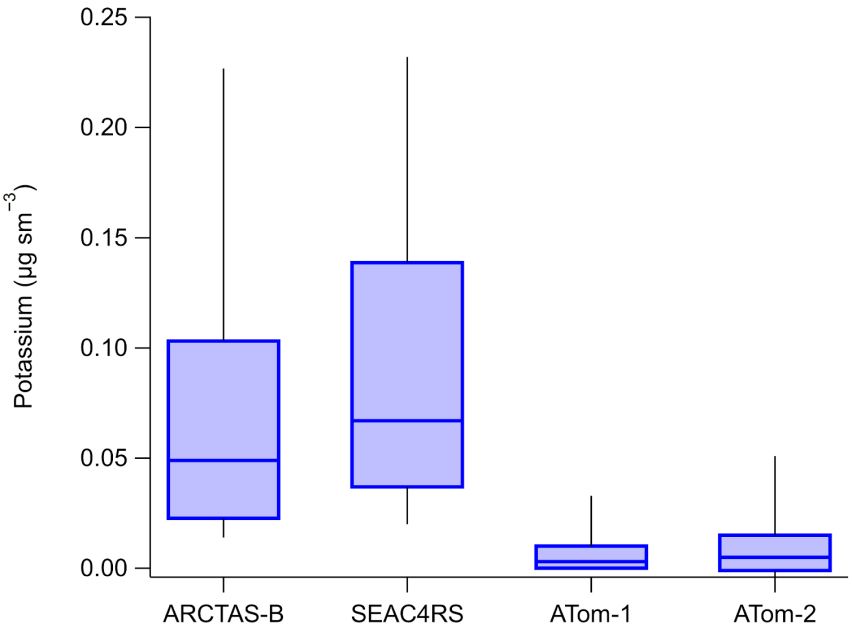

Supplemental Figure 15. ***Comparison of potassium mass concentrations from various campaigns.*** *Box-and-whisker plot for the potassium mass concentration measured during two campaigns focused on biomass burning (ARCTAS-B and SEAC^{4}RS) and two campaigns focused on remote atmosphere (ATom-1 and -2). Potassium was collected onto Teflon filters and analyzed off-line by ion chromatography*[107,108].

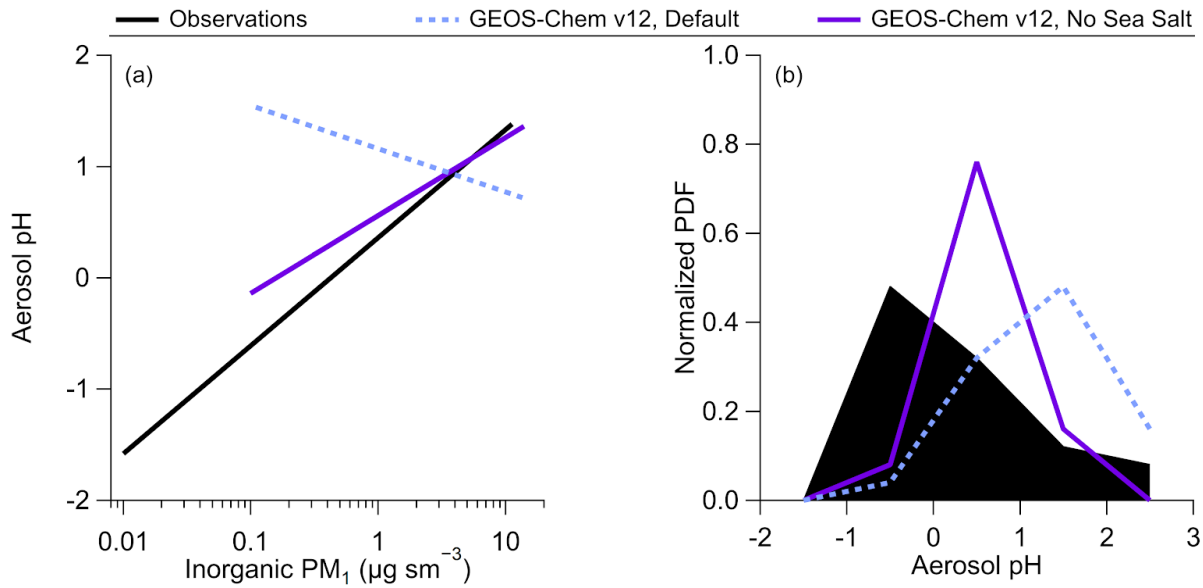

Supplemental Figure 16. ***Investigation in the impacts of removing sea-salt in the calculation of aerosol pH for GEOS-Chem.*** *(a) Comparison of aerosol pH versus log_{10}(inorganic PM_1 (sulfate + nitrate + ammonium)) slopes from observations (black) and default GEOS-Chem (light blue dashed), and GEOS-Chem with sea-salt excluded from the pH calculation (purple) for the boundary layer (surface to 800 hPa). (b) Normalized probability distribution function of aerosol pH for observations (solid black) and default GEOS-Chem and GEOS-Chem with sea-salt excluded for the boundary layer.*

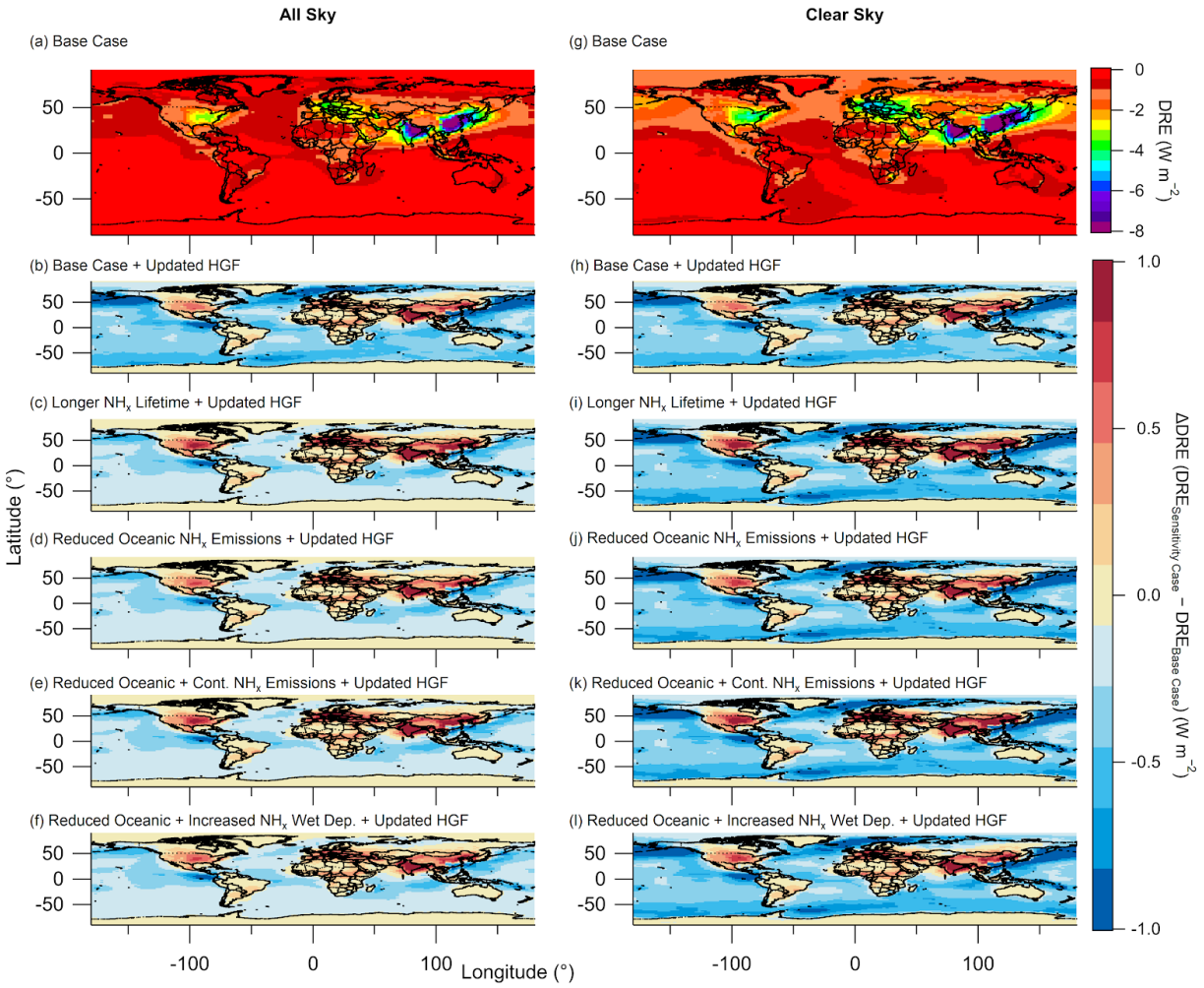

Supplemental Figure 17. ***Changes in the direct radiative effect from the base case with different cases in calculating HGF and ammonium mass concentration.*** *Calculated, annually averaged, short wave direct radiative forcing (DRE) from sulfate, nitrate, and ammonium (and associated water), from GEOS-Chem, for all sky (left column) and clear sky (right column) (a,g) Base Case, (b,h) Base Case with updated HGF, (c,i) decreased Henry's law constant (H) for increased wet deposition lifetime with updated HGF, (d,j) reduced NH_x oceanic emissions with updated HGF, (e,k) reduced NH_x oceanic and continental emissions with updated HGF, and (f,l) reduced NH_x oceanic emissions, increased Henry's law constant (H) for decreased wet deposition lifetime, and updated HGF. See Supplemental Table 7 for description of the different cases and* Fig. 7 *for annual average DRE.*

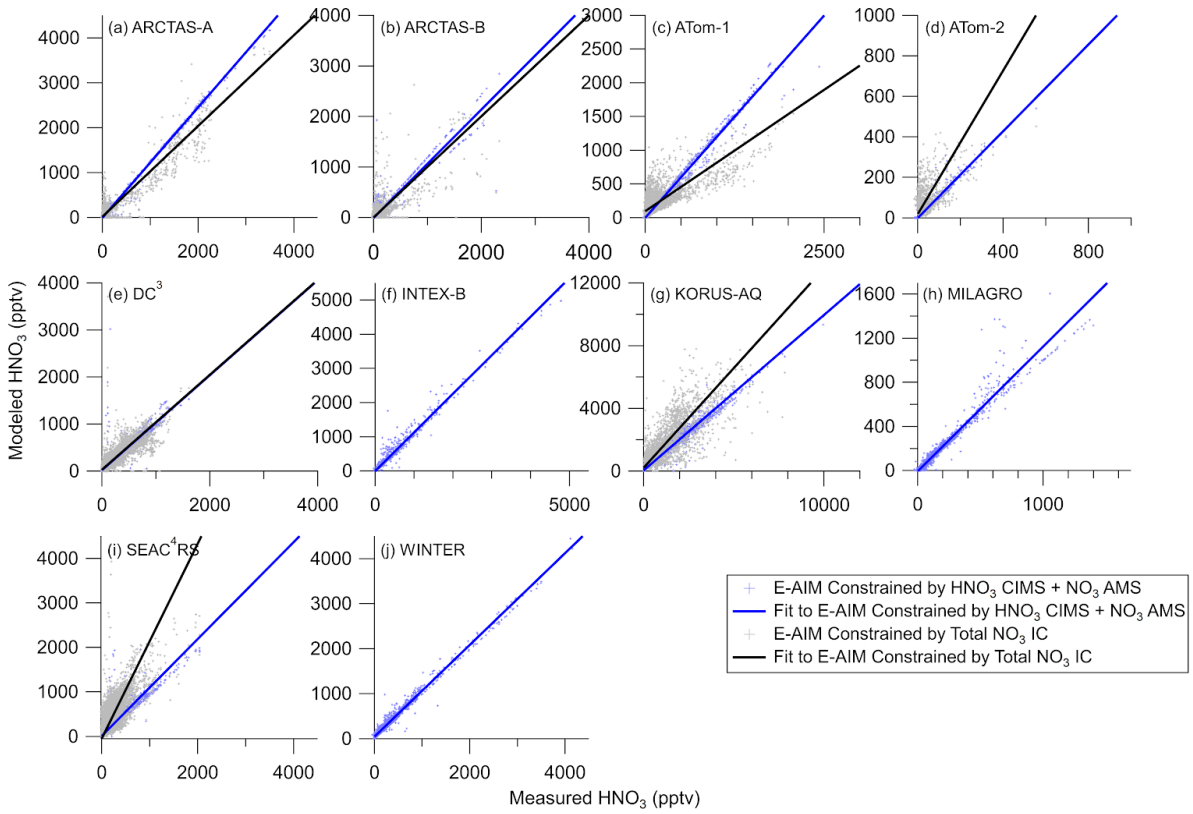

538

539 *Supplemental Figure 18.* ***Comparison of E-AIM predicted and observed nitric acid from all***
540 ***campaigns.*** *Scatter plot of modeled (E-AIM) versus measured gas-phase HNO_3 for the*
541 *campaigns used here (Supplemental Table 2). For campaigns with more than one gas-phase*
542 *HNO_3 measurements (Supplemental Table 3), the comparison of modeled and gas-phase HNO_3*
543 *from the input of both is shown in the scatter plot, where light blue is from CIMS HNO_3 and AMS*
544 *NO_3 and grey is from IC NO_3. For values of the slopes, see Supplemental Figure 20. Regressions*
545 *shown are ODR, where blue is for CIMS + AMS and black is for IC.*

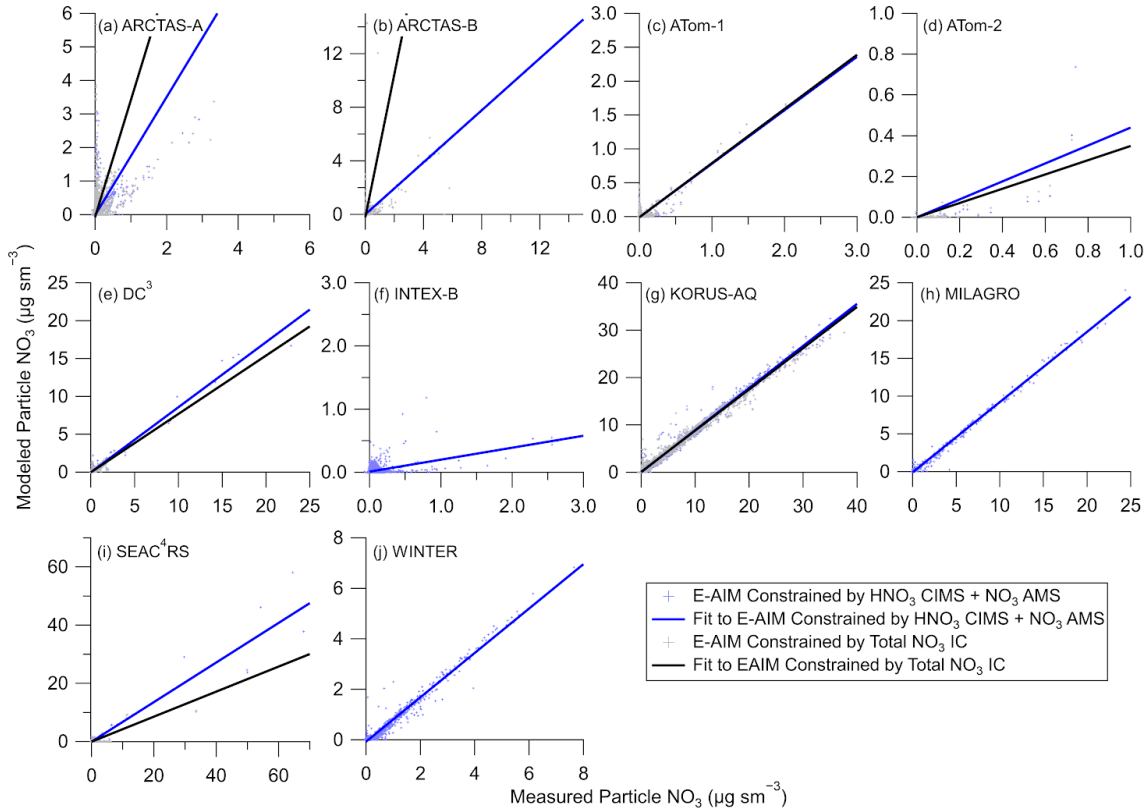

546

547 *Supplemental Figure 19.* ***Comparison of E-AIM predicted and observed nitrate from all***
548 ***campaigns.*** *Same as Supplemental Figure 18, but for particle-phase* NO_3^-*. For values of the*
549 *slopes, see Supplemental Figure 20. Regressions shown are ODR.*

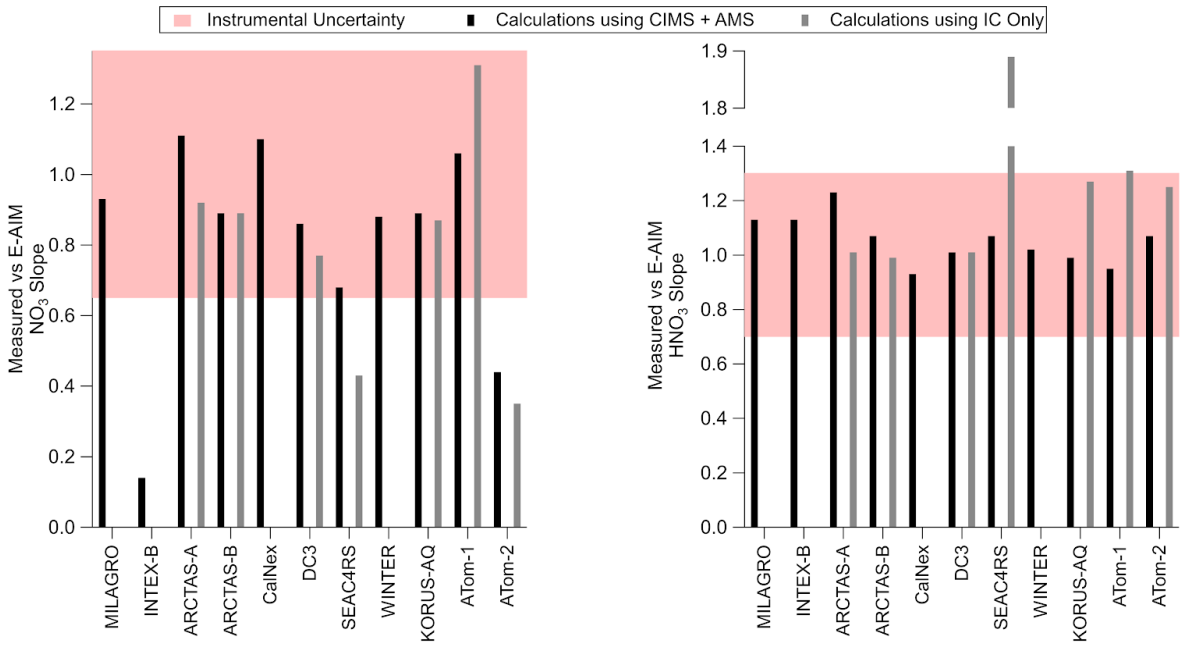

Supplemental Figure 20. ***Comparison of E-AIM predicted and observed nitric acid and nitrate from all campaigns.*** *Comparison of slopes from Supplemental Figure 18 and 19 for the different campaigns along with the uncertainties from the measurements (red shaded) of particle-phase* NO_3^- *and gas-phase* HNO_3*. Black lines are for results using CIMS + AMS and grey is using results from IC only.*

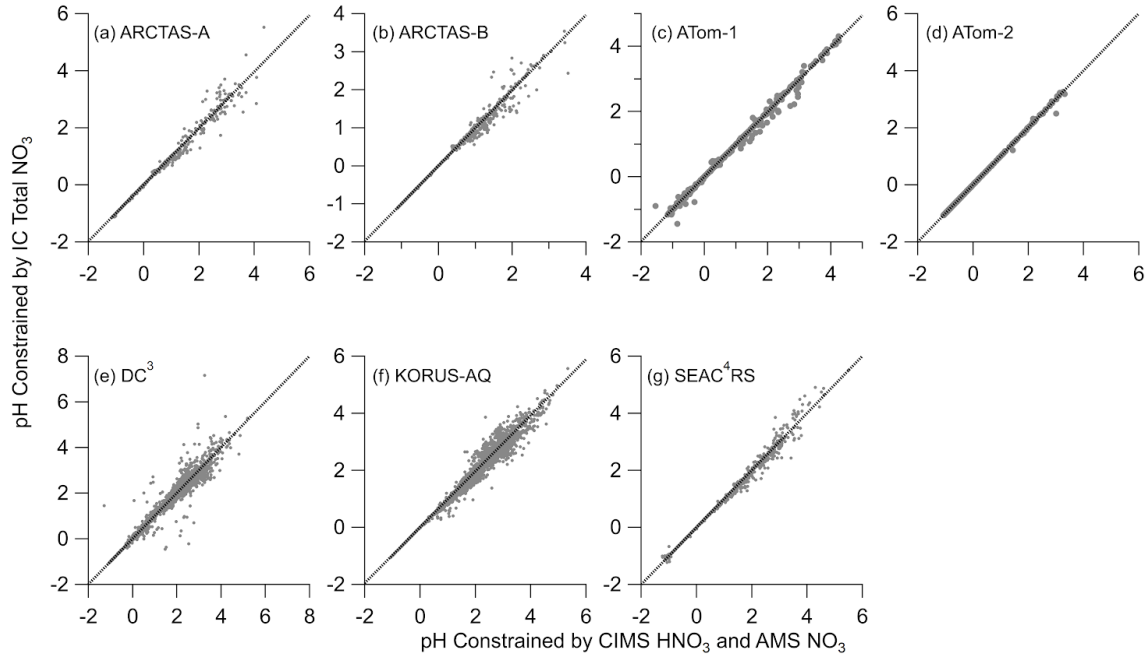

557

558 *Supplemental Figure 21.* ***Comparison of E-AIM predicted pH using different total nitrate***
559 ***inputs.*** *Scatter plot of pH constrained by total nitrate from MC/IC and from CIMS HNO_3 plus*
560 *AMS NO_3. This is only for campaigns where both total nitrate measurements were available*
561 *(Supplemental Table 3). Regressions shown are ODR.*

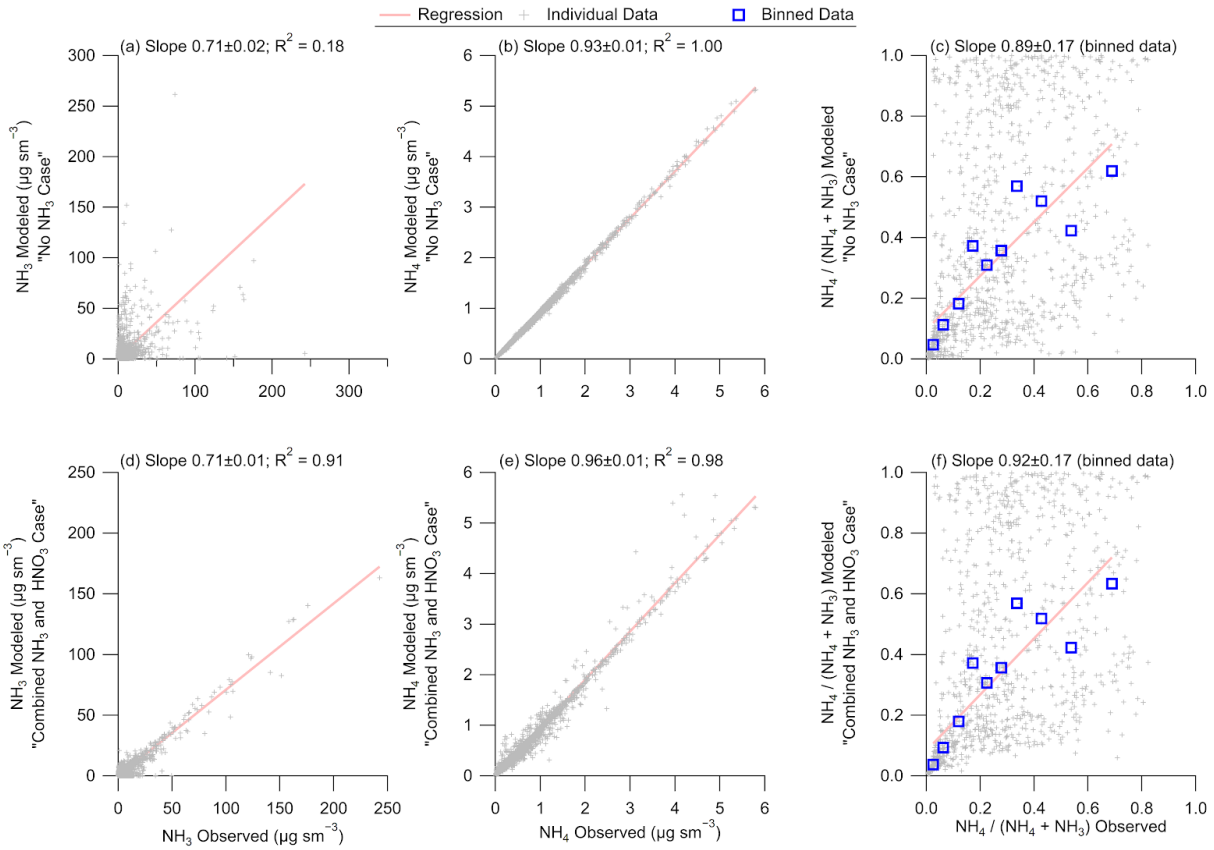

562

563 *Supplemental Figure 22.* ***Evaluation in the performance of E-AIM with and without ammonia***
564 ***as input into the calculations.*** *Evaluation of predicted versus observed ammonia (a and d),*
565 *ammonium (b and e), and fraction of ammonium to total (ammonia plus ammonium) (c and f) for*
566 *E-AIM model constrained without measured ammonia (top) and with measured ammonia*
567 *(bottom). The evaluation is for the CalNex campaign (Supplemental Table 3), the only campaign*
568 *used here that had measurements of ammonia. Regression shown is the least-orthogonal-distance*
569 *regression fitting method (ODR) of the data. Blue squares in (c,f) are binned decile data.*

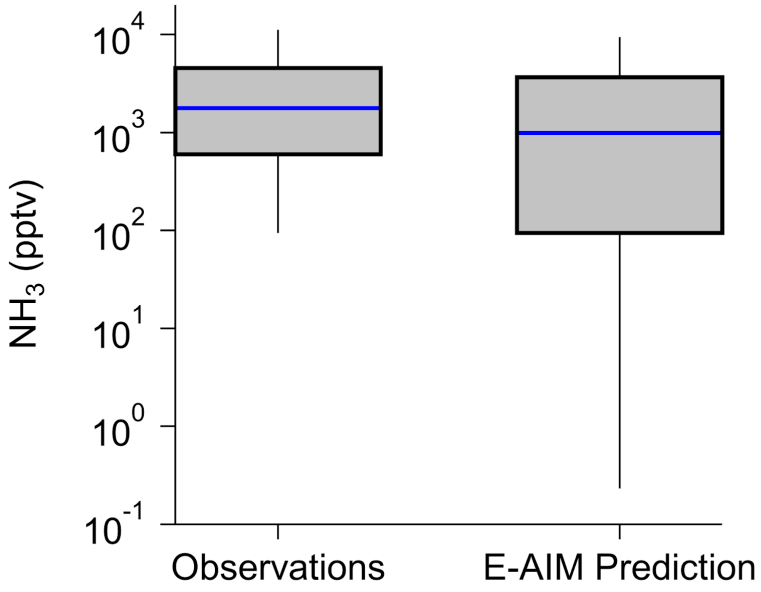

Supplemental Figure 23. ***Comparison of the observed and predicted ammonia during CalNex.*** *Box and whisker plot of observed and E-AIM model ammonia predicted mixing ratios for CalNex. Blue line is the median (50th percentile), box is 25th and 75th percentile, and whisker is the 10th and 90th percentile.*

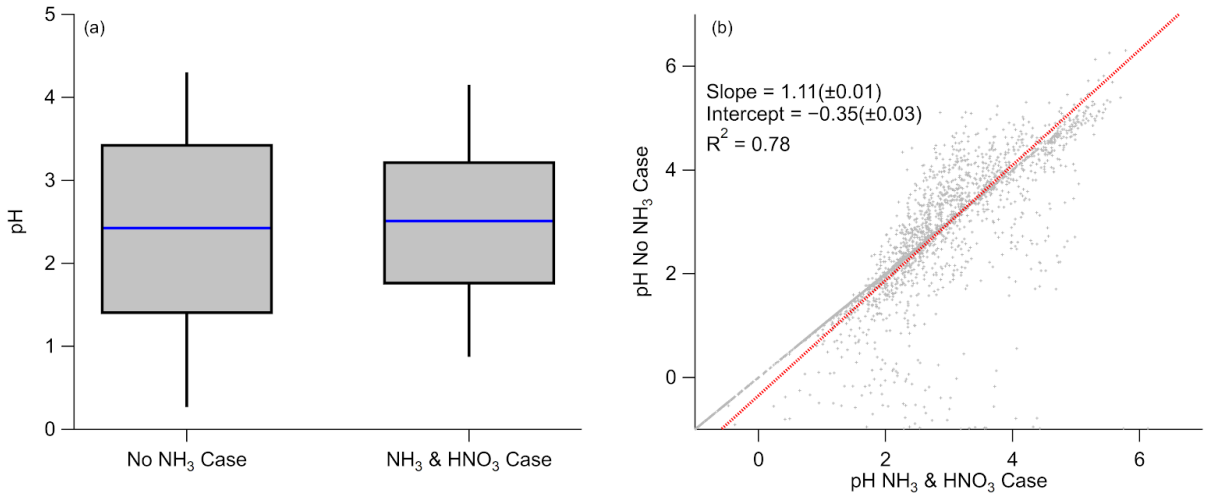

Supplemental Figure 24. ***Comparison in the performance of E-AIM in predicting pH with and without ammonia as input.*** *(a) Box and whisker plot of predicted pH from CalNex with input not including and including gas-phase ammonia. The blue line is the median (50th percentile), box uses the 25th and 75th percentiles, and the whiskers are the 10th and 90th percentile. (b) Scatter plot of the two cases, where the regression is ODR. Red line is the fit.*

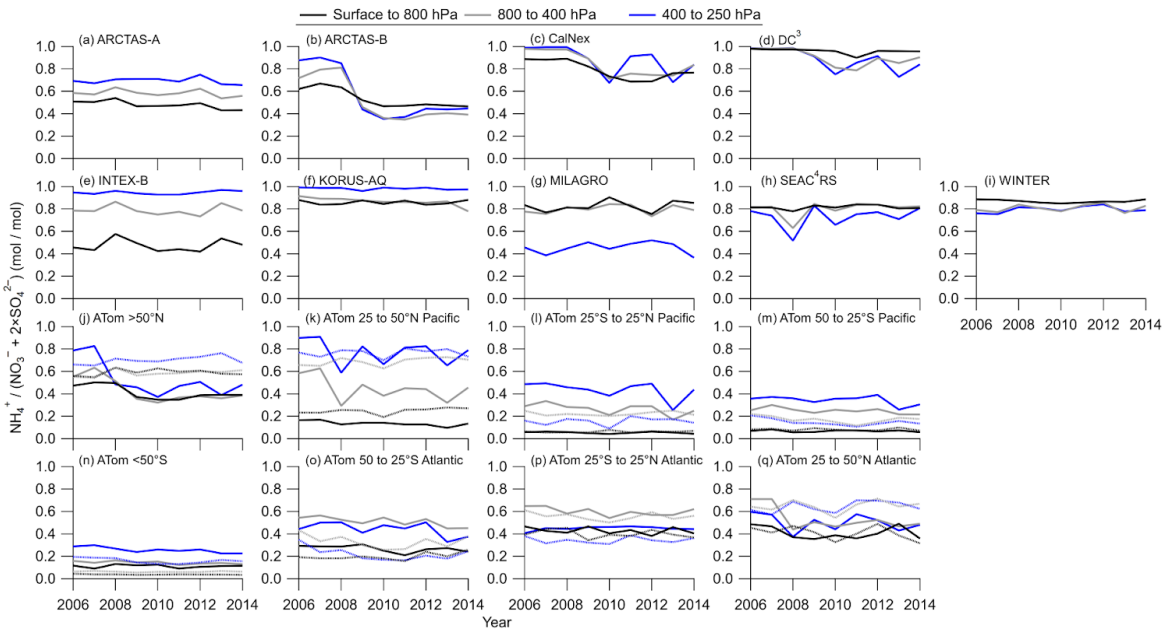

581

582 *Supplemental Figure 25.* ***Evaluation in the predicted trends of ammonium balance over a***
583 ***decade with emissions constant.*** *NH_{4_Bal}, from GEOS-Chem, from 2006 to 2014, with emissions*
584 *for 2010, for the three pressure levels in the troposphere (surface to 800 (black), 800 to 400*
585 *(grey), and 400 to 250 (blue) hPa), for the regions defined in Supplemental Table 2. For the*
586 *ATom regions, solid is for ATom-1 and dashed is for ATom-2.*

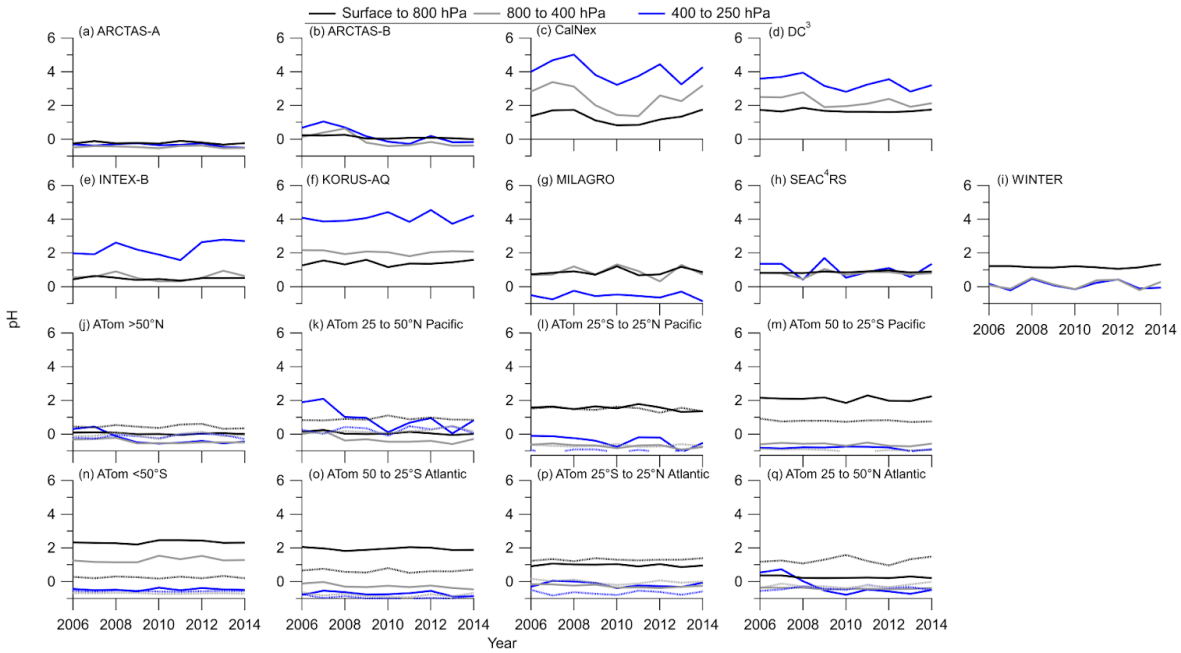

587

588 *Supplemental Figure 26.* ***Evaluation in the predicted trends of pH over a decade with emissions***
589 ***constant.*** *Same as Supplemental Figure 25. pH, from GEOS-Chem, from 2006 to 2014, with*
590 *emissions for 2010, for the three pressure levels in the troposphere (surface to 800 (black), 800*
591 *to 400 (grey), and 400 to 250 (blue) hPa), for the regions defined in Supplemental Table 2. For*
592 *the ATom regions, solid is for ATom-1 and dashed is for ATom-2.*

593 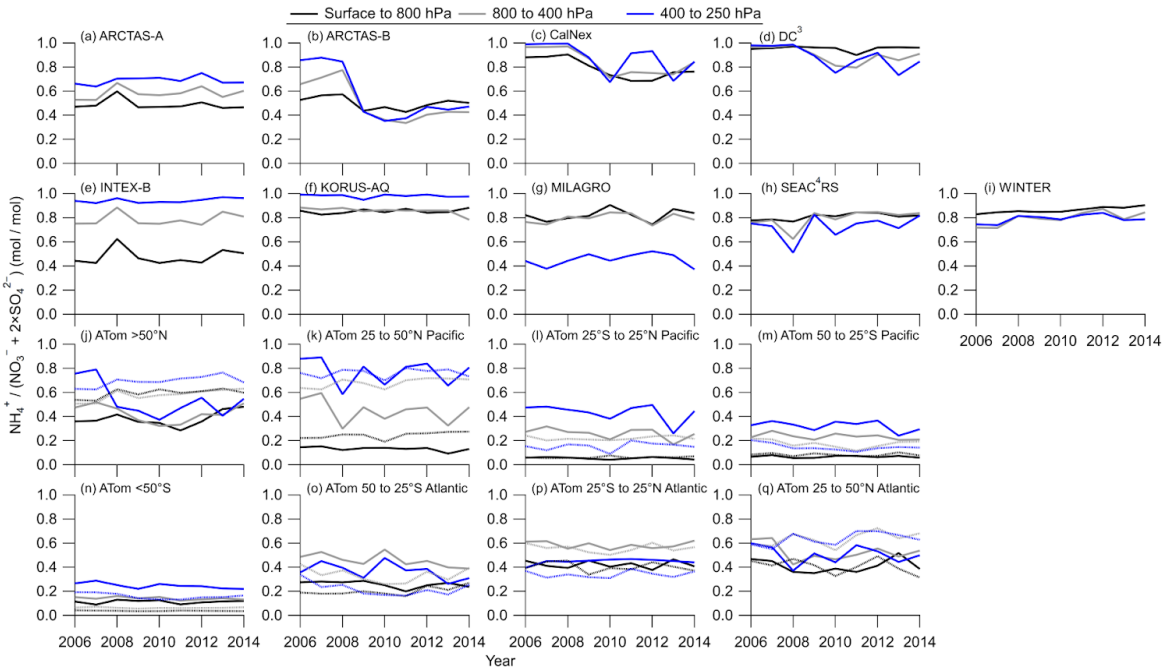

594 *Supplemental Figure 27.* ***Evaluation in the predicted trends of ammonium balance over a***
595 ***decade with meteorology constant.*** *NH_{4_Bal}, from GEOS-Chem, from 2006 to 2014, with constant*
596 *meteorology (2010) but varying emissions, for the three pressure levels in the troposphere*
597 *(surface to 800 (black), 800 to 400 (grey), and 400 to 250 (blue) hPa), for the regions defined in*
598 *Supplemental Table 2. For the ATom regions, solid is for ATom-1 and dashed is for ATom-2.*

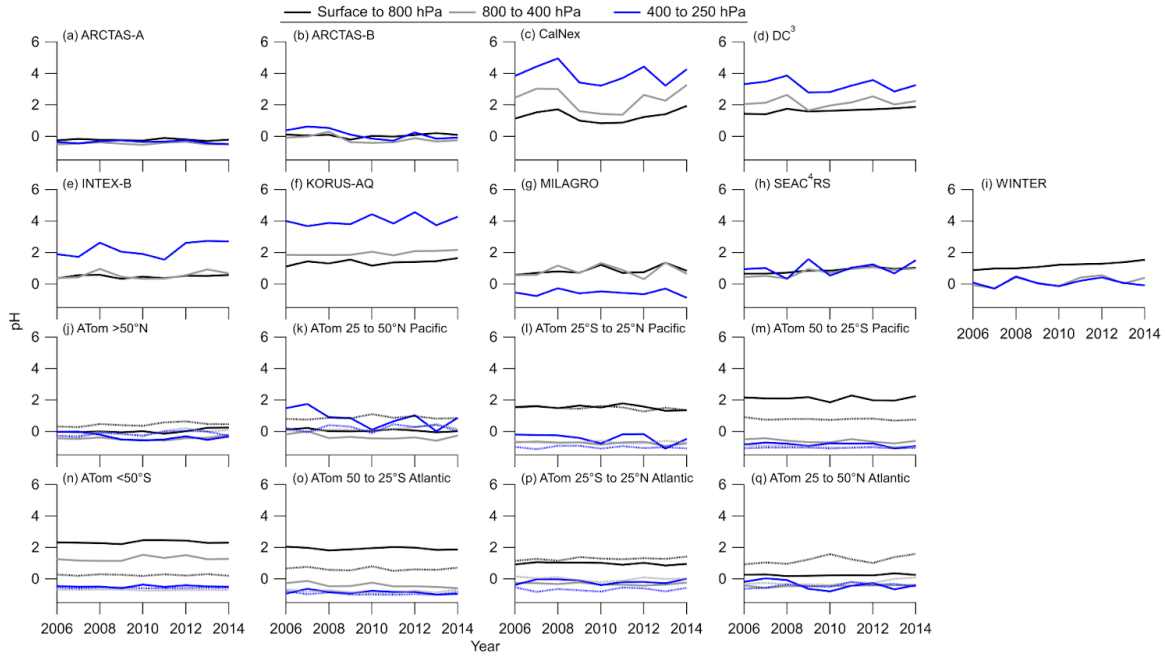

599

600 *Supplemetnal Figure 28.* ***Evaluation in the predicted trends of pH over a decade with***
601 ***meteorology constant.*** *Same as Supplemental Figure 26. pH, from GEOS-Chem, from 2006 to*
602 *2014, with constant meteorology (2010) but varying emissions, for the three pressure levels in*
603 *the troposphere (surface to 800 (black), 800 to 400 (grey), and 400 to 250 (blue) hPa), for the*
604 *regions defined in Supplemental Table 2. For the ATom regions, solid is for ATom-1 and dashed*
605 *is for ATom-2.*

606

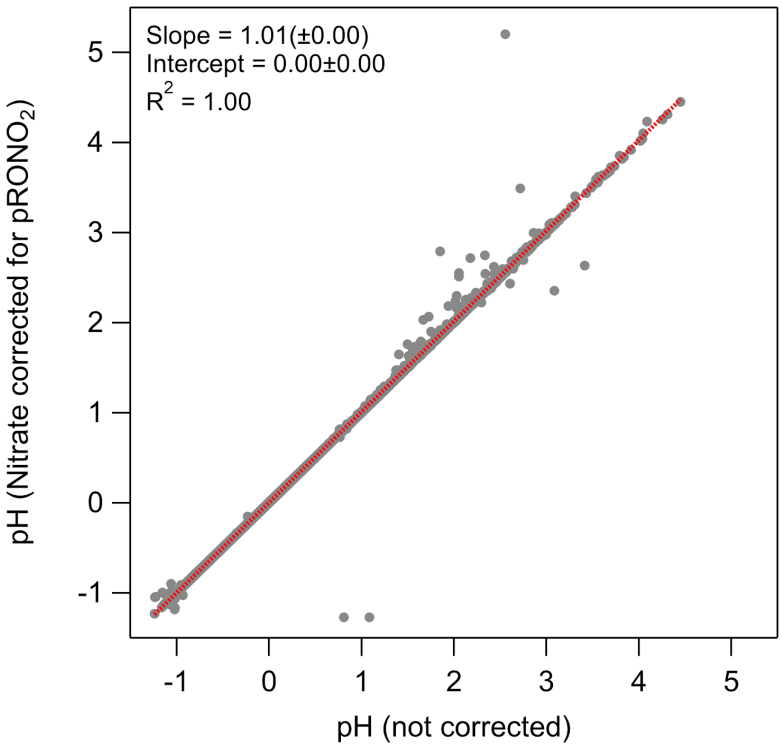

607 *Supplemetnal Figure 29.* ***Comparison of pH from E-AIM with and without accounting for***
608 ***organic nitrate in the mass concentration.*** *Scatter plot of aerosol pH, for SEAC*^{4}*RS, comparing*
609 *pH, where nitrate was corrected for organic oxidized nitrate (pRONO*$_2$*, left axis)*[44] *versus the pH*
610 *reported here. The regression is ODR and shown in red*

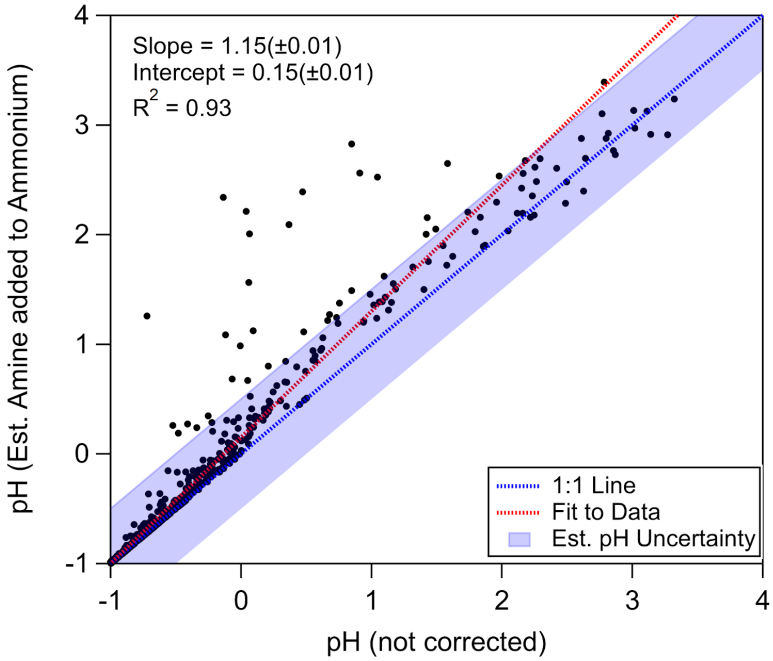

611

612 *Supplemental Figure 30.* ***Comparison of pH from E-AIM with and without accounting for***
613 ***reduced organic amines/amides in the mass concentration.*** *Scatter plot of aerosol pH, for*
614 *ATom-2,where ammonium was corrected for estimated amines (left axis) versus the pH reported*
615 *here. The shaded area represents the ±0.5 pH unit uncertainty estimated from prior studies*[62,63].
616 *Blue dashed is the 1:1 line and red dashed is the fit to the data.*

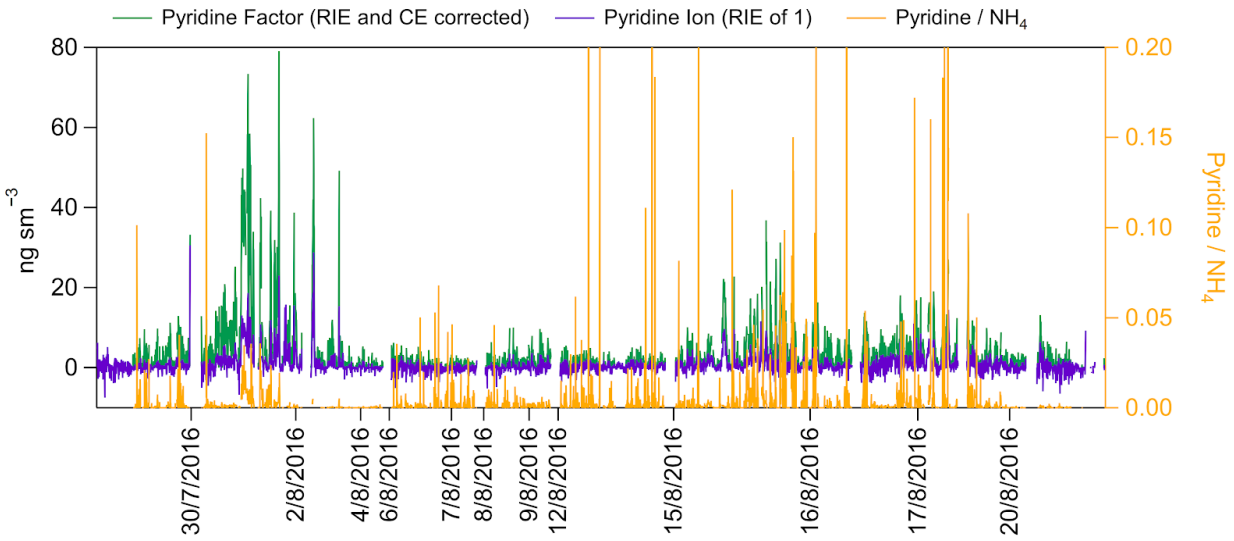

617

618 *Supplemental Figure 31.* ***Time series of pyridine for during ATom-1.*** *(left) Time series of*
619 *pyridine, observed by the AMS, during ATom-1, either by the ion ($C_5H_5N^+$, purple) or positive*
620 *matrix factorization (green)[109]. (right) Ratio of the pyridine mass concentration, from the positive*
621 *matrix factorization result, to the total ammonium mass concentration (orange).*

Supplementary References

1. Dentener, F. J. & Crutzen, P. J. A three-dimensional model of the global ammonia cycle. *J. Atmos. Chem.* **19**, 331–369 (1994).
2. Kürten, A. *et al.* Experimental particle formation rates spanning tropospheric sulfuric acid and ammonia abundances, ion production rates, and temperatures. *J. Geophys. Res. D: Atmos.* **121**, (2016).
3. Wang, M. *et al.* Rapid growth of new atmospheric particles by nitric acid and ammonia condensation. *Nature* **581**, 184–189 (2020).
4. Paulot, F. *et al.* Global oceanic emission of ammonia: Constraints from seawater and atmospheric observations. *Global Biogeochem. Cycles* **29**, 1165–1178 (2015).
5. Williamson, C. J. *et al.* A large source of cloud condensation nuclei from new particle formation in the tropics. *Nature* **574**, 399–403 (2019).
6. Sutton, M. A. *et al.* Towards a climate-dependent paradigm of ammonia emission and deposition. *Philos. Trans. R. Soc. Lond. B Biol. Sci.* **368**, 20130166 (2013).
7. Ge, C., Zhu, C., Francisco, J. S., Zeng, X. C. & Wang, J. A molecular perspective for global modeling of upper atmospheric NH_3 from freezing clouds. *Proc. Natl. Acad. Sci. U. S. A.* **115**, 6147–6152 (2018).
8. Höpfner, M. *et al.* First detection of ammonia (NH_3) in the Asian summer monsoon upper troposphere. *Atmos. Chem. Phys.* **16**, 14357–14369 (2016).
9. Höpfner, M. *et al.* Ammonium nitrate particles formed in upper troposphere from ground ammonia sources during Asian monsoons. *Nat. Geosci.* **12**, 608–612 (2019).
10. Wang, J., Jacob, D. J. & Martin, S. T. Sensitivity of sulfate direct climate forcing to the

hysteresis of particle phase transitions. *J. Geophys. Res.* **113**, 13791 (2008).

11. Salcedo, D. *et al.* Characterization of ambient aerosols in Mexico City during the MCMA-2003 campaign with Aerosol Mass Spectrometry: results from the CENICA Supersite. *Atmos. Chem. Phys.* **6**, 925–946 (2006).
12. *CRC Handbook of Chemistry and Physics, 100th Edition, 2019 - 2020*. 1532 (Taylor & Francis Group, 2019).
13. Heald, C. L. *et al.* Contrasting the direct radiative effect and direct radiative forcing of aerosols. *Atmos. Chem. Phys.* **14**, 5513–5527 (2014).
14. Murphy, J. G. *et al.* Observational constraints on particle acidity using measurements and modelling of particles and gases. *Faraday Discuss.* **200**, 379–395 (2017).
15. Guo, H. *et al.* Evaluating the Consistency of All Submicron Aerosol Mass Measurements (Total and Speciated) for the NASA Atmospheric Tomography Aircraft Mission. (May 4 - 8, 2020) doi:10.5194/egusphere-egu2020-11863.
16. Ovadnevaite, J. *et al.* On the effect of wind speed on submicron sea salt mass concentrations and source fluxes. *J. Geophys. Res. D: Atmos.* **117**, 1–11 (2012).
17. Brock, C. A. *et al.* Aerosol size distributions during the Atmospheric Tomography Mission (ATom): methods, uncertainties, and data products. *Atmos. Meas. Tech.* **12**, 3081–3099 (2019).
18. Kupc, A., Williamson, C., Wagner, N. L., Richardson, M. & Brock, C. A. Modification, calibration, and performance of the Ultra-High Sensitivity Aerosol Spectrometer for particle size distribution and volatility measurements during the Atmospheric Tomography Mission (ATom) airborne campaign. *Atmos. Meas. Tech.* **11**, 369–383 (2018).

19. Guo, H., Nenes, A. & Weber, R. J. The underappreciated role of nonvolatile cations in aerosol ammonium-sulfate molar ratios. *Atmos. Chem. Phys.* **18**, 17307–17323 (2018).
20. Guo, H. *et al.* The Importance of Size Ranges in Intercomparison of Aerosol Volume Concentration Measurements: A Case Study for Aerosol Mass Spectrometer in the ATom Mission. *Atmos. Meas. Tech. Discuss.* **In Review**, (2020).
21. Murphy, D. M. *et al.* The distribution of sea-salt aerosol in the global troposphere. *Atmos. Chem. Phys.* **19**, 4903–4104 (2019).
22. Gaston, C. J., Pratt, K. A., Qin, X. & Prather, K. A. Real-Time detection and mixing state of methanesulfonate in single particles at an inland urban location during a phytoplankton bloom. *Environ. Sci. Technol.* **44**, 1566–1572 (2010).
23. Gaston, C. J. *et al.* The Cloud Nucleating Properties and Mixing State of Marine Aerosols Sampled along the Southern California Coast. *Atmosphere* **9**, 52 (2018).
24. Ault, A. P. *et al.* Size-dependent changes in sea spray aerosol composition and properties with different seawater conditions. *Environ. Sci. Technol.* **47**, 5603–5612 (2013).
25. Palm, B. B. *et al.* In situ secondary organic aerosol formation from ambient pine forest air using an oxidation flow reactor. *Atmos. Chem. Phys.* **16**, 2943–2970 (2016).
26. Fuchs, N. A. & Sutugin, A. G. High-Dispersed Aerosols. in *Topics in Current Aerosol Research* (eds. Hidy, G. M. & Brock, J. R.) (Pergamon, 1971).
27. Seinfeld, J. H. & Pandis, S. N. *Atmospheric Chemistry and Physics: From Air Pollution to Climate Change*. 1232 (John Wiley & Sons, Inc., 2006).
28. Katich, J. M. *et al.* Strong Contrast in Remote Black Carbon Aerosol Loadings Between the Atlantic and Pacific Basins. *J. Geophys. Res. D: Atmos.* **123**, 151 (2018).

29. Park, K., Kittelson, D. B., Zachariah, M. R. & McMurry, P. H. Measurement of Inherent Material Density of Nanoparticle Agglomerates. *J. Nanopart. Res.* **6**, 267–272 (2004).
30. Froyd, K. D. *et al.* A new method to quantify mineral dust and other aerosol species from aircraft platforms using single-particle mass spectrometry. *Atmos. Meas. Tech.* **12**, 6209–6239 (2019).
31. Faloona, I. Sulfur processing in the marine atmospheric boundary layer: A review and critical assessment of modeling uncertainties. *Atmos. Environ.* **43**, 2841–2854 (2009).
32. Prather, K. A. *et al.* Bringing the ocean into the laboratory to probe the chemical complexity of sea spray aerosol. *Proc. Natl. Acad. Sci. U. S. A.* **110**, 7550–7555 (2013).
33. Pye, H. O. T. *et al.* Effect of changes in climate and emissions on future sulfate-nitrate-ammonium aerosol levels in the United States. *J. Geophys. Res.* **114**, 1097 (2009).
34. Jaeglé, L., Quinn, P. K., Bates, T. S., Alexander, B. & Lin, J.-T. Global distribution of sea salt aerosols: new constraints from in situ and remote sensing observations. *Atmos. Chem. Phys.* **11**, 3137–3157 (2011).
35. Ordou, N. & Agranovski, I. E. Mass distribution and elemental analysis of the resultant atmospheric aerosol particles generated in controlled biomass burning processes. *Atmos. Res.* **198**, 108–112 (2017).
36. Hodzic, A. *et al.* Characterization of Organic Aerosol across the Global Remote Troposphere: A comparison of ATom measurements and global chemistry models. *Atmos. Chem. Phys.* **20**, 4607–4635 (2020).
37. Lee, A. K. Y. *et al.* Single-particle characterization of biomass burning organic aerosol

(BBOA): evidence for non-uniform mixing of high molecular weight organics and potassium. *Atmos. Chem. Phys.* **16**, 5561–5572 (2016).

38. Guo, H. *et al.* Fine particle pH and gas–particle phase partitioning of inorganic species in Pasadena, California, during the 2010 CalNex campaign. *Atmos. Chem. Phys.* **17**, 5703–5719 (2017).

39. Keene, W. C. & Savoie, D. L. The pH of deliquesced sea-salt aerosol in polluted marine air. *Geophys. Res. Lett.* **25**, 2181–2184 (1998).

40. Keene, W. C., Pszenny, A. A. P., Maben, J. R. & Sander, R. Variation of marine aerosol acidity with particle size. *Geophys. Res. Lett.* **29**, 1101 (2002).

41. Keene, W. C., Pszenny, A. A. P., Maben, J. R., Stevenson, E. & Wall, A. Closure evaluation of size-resolved aerosol pH in the New England coastal atmosphere during summer. *J. Geophys. Res. D: Atmos.* **109**, (2004).

42. Smith, A. M. *et al.* Ammonia sources, transport, transformation, and deposition in coastal New England during summer. *J. Geophys. Res. D: Atmos.* **112**, (2007).

43. Farmer, D. K. *et al.* Response of an aerosol mass spectrometer to organonitrates and organosulfates and implications for atmospheric chemistry. *Proc. Natl. Acad. Sci. U. S. A.* **107**, 6670–6675 (2010).

44. Fry, J. L. *et al.* Observations of gas- and aerosol-phase organic nitrates at BEACHON-RoMBAS 2011. *Atmos. Chem. Phys.* **13**, 8585–8605 (2013).

45. Huffman, J. a. *et al.* Chemically-resolved aerosol volatility measurements from two megacity field studies. *Atmos. Chem. Phys.* **9**, 7161–7182 (2009).

46. Chen, Y. *et al.* Response of the Aerodyne Aerosol Mass Spectrometer to Inorganic Sulfates

and Organosulfur Compounds: Applications in Field and Laboratory Measurements. *Environ. Sci. Technol.* **53**, 5176–5186 (2019).

47. Kiendler-Scharr, A. *et al.* Ubiquity of organic nitrates from nighttime chemistry in the European submicron aerosol: Organic Nitrates in European PM_1. *Geophys. Res. Lett.* **43**, 7735–7744 (2016).

48. Ng, N. L. *et al.* Nitrate radicals and biogenic volatile organic compounds: oxidation, mechanisms, and organic aerosol. *Atmos. Chem. Phys.* **17**, 2103–2162 (2017).

49. Finewax, Z., de Gouw, J. A. & Ziemann, P. J. Identification and Quantification of 4-Nitrocatechol Formed from OH and NO_3 Radical-Initiated Reactions of Catechol in Air in the Presence of NO_x: Implications for Secondary Organic Aerosol Formation from Biomass Burning. *Environ. Sci. Technol.* **52**, 1981–1989 (2018).

50. Iinuma, Y., Böge, O., Gräfe, R. & Herrmann, H. Methyl-nitrocatechols: atmospheric tracer compounds for biomass burning secondary organic aerosols. *Environ. Sci. Technol.* **44**, 8453–8459 (2010).

51. Liu, X. *et al.* Airborne measurements of western U.S. wildfire emissions: Comparison with prescribed burning and air quality implications. *J. Geophys. Res. D: Atmos.* **122**, 6108–6129 (2017).

52. Liu, X. *et al.* Agricultural fires in the southeastern U.S. during $SEAC^4RS$: Emissions of trace gases and particles and evolution of ozone, reactive nitrogen, and organic aerosol. *J. Geophys. Res. D: Atmos.* **121**, 7383–7414 (2016).

53. Fisher, J. A. *et al.* Organic nitrate chemistry and its implications for nitrogen budgets in an isoprene- and monoterpene-rich atmosphere: Constraints from aircraft ($SEAC^4RS$) and

754 ground-based (SOAS) observations in the Southeast US. *Atmos. Chem. Phys.* **16**, (2016).
755 54. Darer, A. I., Cole-Filipiak, N. C., O'Connor, A. E. & Elrod, M. J. Formation and stability of
756 atmospherically relevant isoprene-derived organosulfates and organonitrates. *Environ. Sci.*
757 *Technol.* **45**, 1895–1902 (2011).
758 55. Nault, B. A. *et al.* Secondary Organic Aerosol Production from Local Emissions Dominates
759 the Organic Aerosol Budget over Seoul, South Korea, during KORUS-AQ. *Atmos. Chem.*
760 *Phys.* **18**, 17769–17800 (2018).
761 56. Almeida, J. *et al.* Molecular understanding of sulphuric acid-amine particle nucleation in
762 the atmosphere. *Nature* **502**, 359–363 (2013).
763 57. Ge, X., Shaw, S. L. & Zhang, Q. Toward understanding amines and their degradation
764 products from postcombustion CO_2 capture processes with aerosol mass spectrometry.
765 *Environ. Sci. Technol.* **48**, 5066–5075 (2014).
766 58. Pyridine. *NIST Chemistry WebBook, SRD 69*
767 https://webbook.nist.gov/cgi/cbook.cgi?ID=C110861&Mask=200#Mass-Spec.
768 59. Ethanamine, N-ethyl-. *NIST Chemistry WebBook, SRD 69*
769 https://webbook.nist.gov/cgi/cbook.cgi?ID=C109897&Mask=200#Mass-Spec.
770 60. Sorooshian, A. *et al.* On the link between ocean biota emissions, aerosol, and maritime
771 clouds: Airborne, ground, and satellite measurements off the coast of California. *Global*
772 *Biogeochem. Cycles* **23**, GB4007 (2009).
773 61. Hodshire, A. L. *et al.* The potential role of methanesulfonic acid (MSA) in aerosol
774 formation and growth and the associated radiative forcings. *Atmos. Chem. Phys.* **19**,
775 3137–3160 (2019).

776 62. Guo, H. *et al.* Fine-particle water and pH in the southeastern United States. *Atmos. Chem.*
777 *Phys.* **15**, 5211–5228 (2015).
778 63. Battaglia, M. A., Jr., Weber, R. J., Nenes, A. & Hennigan, C. J. Effects of Water-soluble
779 Organic Carbon on Aerosol pH. *Atmos. Chem. Phys. Disc.* 1–36 (2019).
780 64. Riva, M. *et al.* Increasing Isoprene Epoxydiol-to-Inorganic Sulfate Aerosol Ratio Results in
781 Extensive Conversion of Inorganic Sulfate to Organosulfur Forms: Implications for Aerosol
782 Physicochemical Properties. *Environ. Sci. Technol.* **53**, 8682–8694 (2019).
783 65. Schueneman, M. K. *et al.* Aerosol pH indicator and organosulfate detectability from
784 Aerosol Mass Spectrometry measurements. *Atmos. Meas. Tech. Discuss.* **Accepted**, (2020).
785 66. Liao, J. *et al.* Airborne measurements of organosulfates over the continental U.S. *J.*
786 *Geophys. Res. D: Atmos.* **120**, 2990–3005 (2015).
787 67. Pye, H. O. T. *et al.* The Acidity of Atmospheric Particles and Clouds. *Atmos. Chem. Phys.*
788 **20**, 4809–4888 (2020).
789 68. Guo, H. *et al.* Fine particle pH and the partitioning of nitric acid during winter in the
790 northeastern United States. *J. Geophys. Res. D: Atmos.* **121**, 10,355–10,376 (2016).
791 69. Gaston, C. J. *et al.* Reactive Uptake of an Isoprene-Derived Epoxydiol to Submicron
792 Aerosol Particles. (2014) doi:10.1021/es5034266.
793 70. Thornton, J. A., Jaeglé, L. & McNeill, V. F. Assessing known pathways for HO_2 loss in
794 aqueous atmospheric aerosols: Regional and global impacts on tropospheric oxidants. *J.*
795 *Geophys. Res. D: Atmos.* **113**, D05303 (2008).
796 71. Meskhidze, N., Chameides, W. L., Nenes, A. & Chen, G. Iron mobilization in mineral dust:
797 Can anthropogenic SO_2 emissions affect ocean productivity? *Geophys. Res. Lett.* **30**, 2085

(2003).

72. Ackendorf, J. M., Ippolito, M. G. & Galloway, M. M. pH Dependence of the Imidazole-2-carboxaldehyde Hydration Equilibrium: Implications for Atmospheric Light Absorbance. *Environ. Sci. Technol. Lett.* **4**, 551–555 (2017).

73. Losey, D. J., Ott, E.-J. E. & Freedman, M. A. Effects of High Acidity on Phase Transitions of an Organic Aerosol. *J. Phys. Chem. A* **122**, 3819–3828 (2018).

74. Molina, L. T. *et al.* An overview of the MILAGRO 2006 Campaign: Mexico City emissions and their transport and transformation. *Atmos. Chem. Phys.* **10**, 8697–8760 (2010).

75. Singh, H. B., Brune, W. H., Crawford, J. H., Flocke, F. & Jacob, D. J. Chemistry and transport of pollution over the Gulf of Mexico and the Pacific: spring 2006 INTEX-B campaign overview and first results. *Atmos. Chem. Phys.* **9**, 2301–2318 (2009).

76. Jacob, D. J. *et al.* The Arctic Research of the Composition of the Troposphere from Aircraft and Satellites (ARCTAS) mission: design, execution, and first results. *Atmos. Chem. Phys.* **10**, 5191–5212 (2010).

77. Ryerson, T. B. *et al.* The 2010 California Research at the Nexus of Air Quality and Climate Change (CalNex) field study. *J. Geophys. Res. D: Atmos.* **118**, 5830–5866 (2013).

78. Barth, M. C. *et al.* The Deep Convective Clouds and Chemistry (DC3) Field Campaign. *Bull. Am. Meteorol. Soc.* **96**, 1281–1309 (2015).

79. Toon, O. B. *et al.* Planning, implementation, and scientific goals of the Studies of Emissions and Atmospheric Composition, Clouds and Climate Coupling by Regional Surveys (SEAC^{4}RS) field mission. *J. Geophys. Res. D: Atmos.* **121**, 4967–5009 (2016).

80. Schroder, J. C. *et al.* Sources and Secondary Production of Organic Aerosols in the

Northeastern US during WINTER. *J. Geophys. Res. D: Atmos.* (2018) doi:10.1029/2018JD028475.

81. Jordan, C. E. *et al.* Investigation of factors controlling PM2.5 variability across the South Korean Peninsula during KORUS-AQ. *Elementa: Science of the Anthropocene* **8**, (2020).

82. DeCarlo, P. F. *et al.* Field-deployable, high-resolution, time-of-flight aerosol mass spectrometer. *Anal. Chem.* **78**, 8281–8289 (2006).

83. DeCarlo, P. F. *et al.* Fast airborne aerosol size and chemistry measurements above Mexico City and Central Mexico during the MILAGRO campaign. *Atmos. Chem. Phys.* **8**, 4027–4048 (2008).

84. Crounse, J. D., McKinney, K. A., Kwan, A. J. & Wennberg, P. O. Measurement of Gas-Phase Hydroperoxides by Chemical Ionization Mass Spectrometry. *Anal. Chem.* **78**, 6726–6732 (2006).

85. Dunlea, E. J. *et al.* Evolution of Asian aerosols during transpacific transport in INTEX-B. *Atmos. Chem. Phys.* **9**, 7257–7287 (2009).

86. Cubison, M. J. *et al.* Effects of aging on organic aerosol from open biomass burning smoke in aircraft and laboratory studies. *Atmos. Chem. Phys.* **11**, 12049–12064 (2011).

87. Talbot, R. W. *et al.* Large-scale distributions of tropospheric nitric, formic, and acetic acids over the western Pacific basin during wintertime. *J. Geophys. Res.: Atmos.* **102**, 28303–28313 (1997).

88. Drewnick, F. *et al.* A New Time-of-Flight Aerosol Mass Spectrometer (TOF-AMS)—Instrument Description and First Field Deployment. *Aerosol Sci. Technol.* **39**, 637–658 (2005).

89. Bahreini, R. *et al.* Gasoline emissions dominate over diesel in formation of secondary organic aerosol mass. *Geophys. Res. Lett.* **39**, L06805 (2012).

90. Nowak, J. B. *et al.* Airborne observations of ammonia and ammonium nitrate formation over Houston, Texas. *J. Geophys. Res.* **115**, 2706 (2010).

91. Neuman, J. A. *et al.* Fast-response airborne in situ measurements of HNO_3 during the Texas 2000 Air Quality Study. *J. Geophys. Res.* **107**, 4436 (2002).

92. Lee, B. H. *et al.* An Iodide-Adduct High-Resolution Time-of-Flight Chemical-Ionization Mass Spectrometer: Application to Atmospheric Inorganic and Organic Compounds. *Environ. Sci. Technol.* **48**, 6309–6317 (2014).

93. Tsigaridis, K. *et al.* The AeroCom evaluation and intercomparison of organic aerosol in global models. *Atmos. Chem. Phys.* **14**, 10845–10895 (2014).

94. Marais, E. A. *et al.* Aqueous-phase mechanism for secondary organic aerosol formation from isoprene: application to the southeast United States and co-benefit of SO_2 emission controls. *Atmos. Chem. Phys.* **16**, 1603–1618 (2016).

95. Jo, D. S. *et al.* A simplified parameterization of isoprene-epoxydiol-derived secondary organic aerosol (IEPOX-SOA) for global chemistry and climate models: a case study with GEOS-Chem v11-02-rc. *Geosci. Model Dev.* **12**, 2983–3000 (2019).

96. Bian, H. *et al.* Investigation of global particulate nitrate from the AeroCom phase III experiment. *Atmos. Chem. Phys.* **17**, 12911–12940 (2017).

97. Kodros, J. K. & Pierce, J. R. Important global and regional differences in aerosol cloud-albedo effect estimates between simulations with and without prognostic aerosol microphysics. *J. Geophys. Res. D: Atmos.* **122**, 4003–4018 (2017).

98. Horowitz, L. W. *et al.* The GFDL Global Atmospheric Chemistry-Climate Model AM4.1: Model Description and Simulation Characteristics. *J. Adv. Model. Earth Syst.* (2020) doi:10.1029/2019MS002032.

99. Müller, C. *et al.* Seasonal variation of aliphatic amines in marine sub-micrometer particles at the Cape Verde islands. *Atmos. Chem. Phys.* **9**, 9587–9597 (2009).

100. van Pinxteren, M. *et al.* Chemical characterization of sub-micrometer aerosol particles in the tropical Atlantic Ocean: marine and biomass burning influences. *J. Atmos. Chem.* **72**, 105–125 (2015).

101. Frossard, A. A. *et al.* Sources and composition of submicron organic mass in marine aerosol particles: Marine Aerosol Organic Mass Composition. *J. Geophys. Res. D: Atmos.* **119**, 12,977–13,003 (2014).

102. Youn, J.-S., Crosbie, E., Maudlin, L. C., Wang, Z. & Sorooshian, A. Dimethylamine as a major alkyl amine species in particles and cloud water: Observations in semi-arid and coastal regions. *Atmos. Environ.* **122**, 250–258 (2015).

103. Gibb, S. W., Mantoura, R. F. C. & Liss, P. S. Ocean-atmosphere exchange and atmospheric speciation of ammonia and methylamines in the region of the NW Arabian Sea. *Global Biogeochem. Cycles* **13**, 161–178 (1999).

104. Facchini, M. C. *et al.* Important source of marine secondary organic aerosol from biogenic amines. *Environ. Sci. Technol.* **42**, 9116–9121 (2008).

105. Huang, S. *et al.* Source apportionment of the organic aerosol over the Atlantic Ocean from 53°N to 53°S: significant contributions from marine emissions and long-range transport. *Atmos. Chem. Phys.* **18**, 18043–18062 (2018).

106. Blake, N. J. *et al.* The seasonal evolution of NMHC's and light alkyl nitrates at middle to northern latitudes during TOPSE. *J. Geophys. Res. D: Atmos.* **108**, 8359 (2003).

107. Dibb, J. E. *et al.* Airborne sampling of aerosol particles: Comparison between surface sampling at Christmas Island and P-3 sampling during PEM-Tropics B. *J. Geophys. Res.* **108**, 8230 (2002).

108. Dibb, J. E. *et al.* Aerosol chemical composition in Asian continental outflow during the TRACE-P campaign: Comparison with PEM-West B. *J. Geophys. Res.: Atmos.* **108**, 8815 (2003).

109. Ulbrich, I. M., Canagaratna, M. R., Zhang, Q., Worsnop, D. R. & Jimenez, J. L. Interpretation of organic components from Positive Matrix Factorization of aerosol mass spectrometric data. *Atmos. Chem. Phys.* **9**, 2891–2918 (2009).